Simulation of Chemical Enrichment in Galaxies

Master Thesis

at the

Ludwig-Maximilians-Universität München

submitted by

Emilio Mevius

supervised by

Dr. Klaus Dolag

Munich, November 2016

Simulation Chemischer Bereicherung in Galaxien

Masterarbeit

an der

Ludwig-Maximilians-Universität München

vorgelegt von

Emilio Mevius

betruet von

Dr. Klaus Dolag

München, November 2016

Abstract

Galaxy formation models distinguish two main modes, how the stellar disc component of spiral galaxies can grow. The disk grows either through formation of stars from newly accreted, mainly pristine material in the outer parts, or by consuming more enriched gas in the disk and grow from the inside out. Indication on which of the processes is dominant can be obtained by observations, especially from the correlation of different galactic properties. Observed radial profiles of the chemical enrichment-level currently support more the inside out model and give additional information of the evolution history. Star formation, gas in- and out-flows are fundamental processes in the evolution of galaxies, and the chemical enrichment, their ashes. The observed chemical enrichment therefore is a key element for understanding galaxy formation and evolution. The correlation between the stellar mass and the chemical content of galaxies is known already for many years and its slope, although not completely understood yet, is probably established by the action of galactic winds, a key player for re-distributing mass and energy from the galactic feedback processes. The mass-metallicity relation (MZR) therefore can be used to constrain different feedback models in numerical simulations. Still, the treatment of detailed chemical enrichment in galaxies within cosmological simulations is a relative new field and many simulations fail to properly reproduce the observed trends and evolution of the chemical enrichment in galaxies. The main goal of this work is to make an up to date comparison of the MZR and the metallicity gradients seen in the latest observational data with the galaxies in the MAGNETICUM simulation, which follow a detailed model of stellar evolution and chemical enrichment, described in Tornatore et. all 2007. This allows us to study the outcome of the simulations and to infer the influence of different feedback models, together with the effects of different numerical resolutions. In addition we compare the influence of using different observational tracer for the metallicity by mimicking the same selection criteria than observations, addressing the possible influence of numerical and observational effects in discrepancies with observed trends, which will help to interpret current and future results in this relatively new field.

Contents

Contents

List of Figures

List of Tables

1 Introduction

1.1 Evolution of Stars

The Hertzsprung-Russell diagram (HRD) represents a universal distribution of stars in a temperature-luminosity matrix. The patterns found in the HRD reveal the paths followed by stars during their evolution. These paths through the HRD depend strongly on the initial mass. Differentiating by initial mass is therefore the best way to portray the different possible stellar evolutions.

The main sequence (MS) is the most obvious trend in the HRD, a nearly diagonal line going from the faint red region to the bright blue one and is the place where live the most of the stars. The left panel in Figure 1.1 shows a typical picture of the HRD, where the main sequence cross through it, together with other recognizable regions.

The Hayashi line is a nearly vertical line on the right side of the HRD that marks the threshold of hydrostatic equilibrium. The position of the line depends on the initial mass. The more massive the stars are, the higher the needed temperature is, to reach the hydrostatic equilibrium. The collapse of the molecular cloud during the birth of a star finish by reaching the Hayashi line. After that, the surface brightness sink with nearly constant temperature until the hydrostatic equilibrium is reached.

The Henyey line appears for massive enough protostars ($\gtrsim 0.5$ M$_\odot$) and represent the way from the Hayashi line to the main sequence. The temperature increase and the luminosity also, slightly. Through the nuclear fusion sink the luminosity again just before to enter the MS. The right panel in Figure 1.1 is portrayed the possible ways of a protostar according to its initial mass.

Having this tool is easier to follow the birth and evolution of stars. Star formation (SF) starts by the gravitational collapse of a molecular cloud, mostly composed by H and He. Magnetic fields and turbulences could affect the stability of the molecular cloud during SF, but their role is still poorly understood. Otherwise, only the pressure out of the hydrostatic conditions acts against the gravitation. The Jeans criterion gives a threshold mass, called Jean's mass M_J, for which the thermic energy cannot counteract the gravitation energy any longer and avoid the gravitational collapse. Under the assumptions of spherical symmetry and constant density, the M_J reaches:

$$M_J = \left(\frac{5kT}{Gm}\right)^{3/2}\left(\frac{3}{4\pi\rho}\right)^{1/2} \tag{1.1}$$

Where k is the Boltzmann constant, T is the temperature, G is the gravitation constant, m is the mass per particle in the cloud and ρ is an assumed constant density. Any molecular cloud with a mass bigger than M_J, should theoretically collapse.

By all matter with a temperature greater than the absolute zero, interatomic collisions cause the
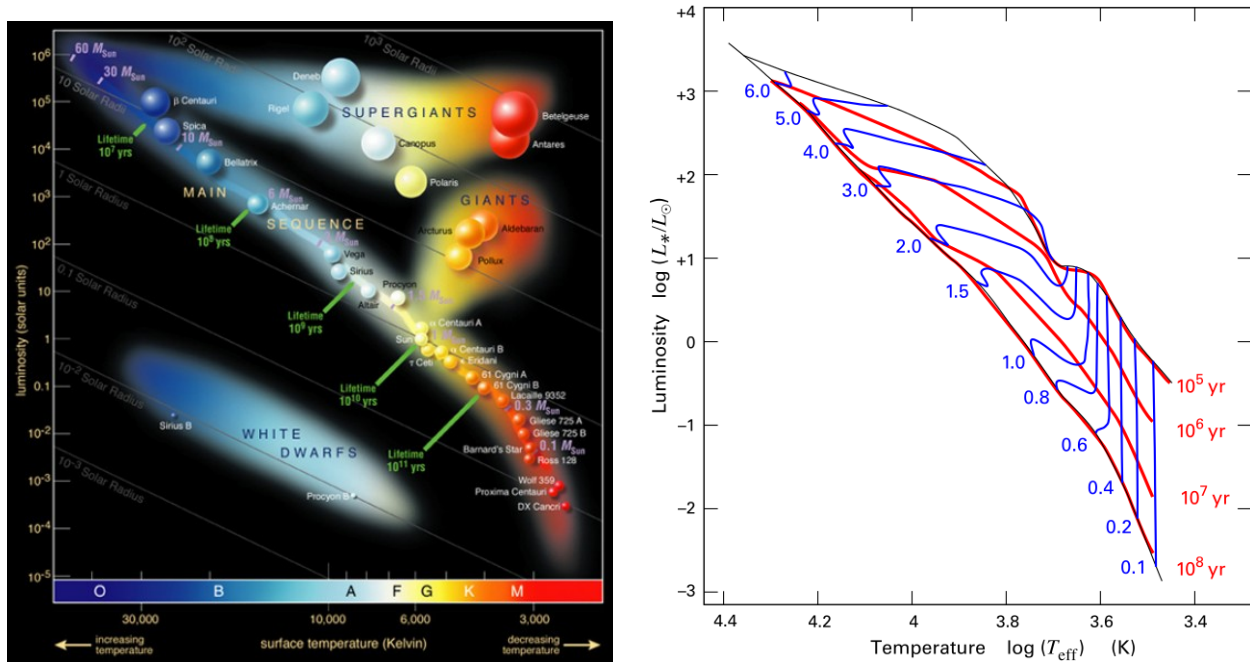
Figure 1.1: *Left: Hertzsprung-Russell diagram showing the position of some known stars. Credits: ESO. Right: Pre-main-sequence evolutionary paths (PMS), i.e. the way to get to the main sequence (MS). The black line placed top right run through the birth places of stars of different masses. The blue lines represent the PMS and the black line placed at the bottom left represents the MS. The end of the path is addressed with the stellar mass in solar units. The nearly vertical blue lines are known as the Hayashi lines, while the nearly horizontal ones as the Henyey lines. As seen in the graphic, taken from Steven and Palla (2008), the most massive stars born directly on the Henyey line and stay there until they reach the MS. Average stars go through the Hayashi line before to turn to the Henyey line. The lightest ones instead, stay on the Hayashi Line until they reach the MS. The red lines represent Isochrones, i.e. lines that connect the points of constant age through the different paths.*

kinetic energy of the atoms to change and set electromagnetic radiation free. This emission is called thermal radiation. The first thermal radiations coming from the conversion of gravitational energy into thermic energy in the core are emitted until the density in the surface increase enough to be optical thick. Before that, just radiative losses are present, i.e. the flux from regions with optical thin layers.

After the outer shells become optical thick, the thermic energy can oppose the gravitational energy and subsequently stops the first collapse. The radius of the first hydrostatic core (FHSC), also called pre-stellar core, reaches 10 to 20 AE for average stars. This free fall phase takes $\sim$ 10000 years until the temperature in the core is big enough to split the H_2 molecules in single H atoms.

The consumed energy for transforming molecular H in atomic H is not used any longer for the stability of the core, starting a second big collapse. A new hydrostatic equilibrium is reached of the same way and the core of the now called protostar reaches only $\sim$ 1.5 $R_\odot$ in average.

From here on, the protostar is victim of the continuous incursion of mass from the surroundings and gains mass. This phase, called main accretion phase, is the key stage to decide if the protostar becomes a star. As star are recognized only the objects, which in this phase reach a temperature high enough to start the nuclear fusion of the H atoms. The fusion of H starts by $\sim 3 \cdot 10^9$ K and this is only possible with an initial stellar mass from ~ 0.07 $M_\odot$ up. Here start the true life of

the stars, if starts. The different life paths depend from here on, on the initial mass.

- **Until $\sim$ 0.3 M$_\odot$** are considered mass poor stars. They stay in the Hayashi line until to reach the MS, as showed in Figure 1.1. The temperature in this case was just enough to start the H fusion, and this keep going the slowest. Red dwarfs can live over 10^{12} years. Almost 2/3 of all stars are red dwarfs. After finally staying without fuel, they contract and reach a diameter of some thousands of km. At this stage the stabilization is only possible through the degenerated pressure of the electrons. The properties of degenerated matter appears hereby when the density is big enough or the temperature low enough, so that the behavior deviates of the classic physics, giving space to quantum physical effects.

- **From $\sim$ 0.3 M$_\odot$ until $\sim$ 2.3 M$_\odot$** are considered sun-like stars. They live around $\sim 10^9$ years. These stars are massive enough to reach enough temperature in the core to start the fusion of He, one of the products of the previous H fusion. All processes overlap, so the He-phase starts when there is still some H in the core and in the shell. Stars are built with shell after shell with the heavier elements going inside out. The He fusion produce enough temperature to fusion the H in the shell and make the star expand. With the expansion of the star and growth of its luminosity, the stars follow a diagonal path in the HRD known as the red giant branch (RGB). There are many branches and subbranches and we review only the most outstanding ones. After the so called *He-flash*, a big energy release raise the temperature of the core at the point that is not degenerated any more. The lower pressure lets the size of the star sink, maintaining the luminosity nearly constant. This produce a nearly horizontal path in the HRD, the horizontal branch (HB). When the He in the core is over, the temperature in the core decrease and the star contracts. The contraction, nevertheless, produce enough temperature for He fusion in the shell, making the star expand and its luminosity grow. This diagonal path is the second most notable path in the HRD after the MS and is known as the asymptotic giant branch (AGB), where red giant stars are placed in the left panel in Figure 1.1. At this point there is H and He almost exclusively in the shell and a burning core of C and O. During this trip is common to lose high amounts of mass from the shell through stellar winds, also called AGB-winds, due to the impossibility to keep maintaining these layers gravitational coupled. *Momentum-driven-winds* are called the stellar winds that carry the momentum of the radiation pressure from continuous absorption and scattering from the stellar activity and nearby SNe. Only the most massive stars form also a so called *planetary nebula* around them. When the fuel of He is finally over, these stars contract and end up as white dwarfs (WD).

- **From $\sim$ 2.3 M$_\odot$ until $\sim$ 3 M$_\odot$**, stars are already able to start the fusion of C. In this mass range is so much mass lost through the AGB-winds, that the Chandrasekhar limit is not reached and they end up as WD as well. This limit ($\sim$ 1.4 M$_\odot$) is the maximum possible mass for a stable WD. As soon as this threshold is reached, the core collapses in matter of seconds and the shell is spread violently away through the energy that is set free mostly in form of neutrinos. This is a so called supernova (SN) explosion. Further details about SN types are given in Section 1.1.1.

- **Over $\sim$ 3 M$_\odot$** is considered the range of the most massive stars. They can consume their whole fuel in just some hundred thousand years. They hike to the region of super giants through their own super giant branch after their short stay in the MS, as can be seen in the left panel in Figure 1.1. The biggest part of the star gather together in a Fe core of $\sim$ 10000 km of diameter until the SN explosion. The core of exploding super massive stars

is only stabilized through a degenerated pressure, in this case of neutrons. This remains, together with WDs, are called *compact objects*, further described in Section 1.1.2.

Is remarkable, that the metals (in Astronomy heavier elements than He) could also play a role during the life of the stars, affecting the duration of the fusion phases as well as the formation of magnetic fields and how strong become the stellar winds. Evolutionary processes related to metallicity in astronomy are in general poorly understood and represent a new field.

1.1.1 Supernovae

Understanding the role of supernovae (SN) is a key step to reproduce the observed chemical enrichment in galaxies. SN explosions represent the principal mechanism to enrich the environment with heavy metals. Together with the stellar winds, define the enrichment, as well as the distribution of the elements by means of the transferred momentum.

The most representative types of SN are the SNIa and SNII

- SNIa: Arises from a binary system with mass in the range 0.8-8 $M_\odot$. Under this variant, a white dwarf (WD) trap another star in his gravitational field and accretes gradual its mass until to reach near exactly the Chandrasekhar limit. Because of the closeness to the theoretical limit where a SN explosion is possible, these events are presumed to have nearly the same mass, expelled energy and luminosity, becoming commonly used standard candles to measure distances in the deep space. After the explosion stays no compact object behind and the partner star is hurled away.

- SNII: Arises with masses of m $\gtrsim$ 8 $M_\odot$. The typical feature to recognize this kind of SN is the appearance of spectral lines of H. This explosion is a natural part in the life of stars with masses above 3 $M_\odot$. They don't need extra accretion of mass from some neighbour star to reach the Chandrasekhar limit.

The contribution of each SN can be understood through the different fusion processes that take place during the life of a star ending up as one type of SN or the other. The most important reaction during the H-phase is called the *triple-alpha process* and produce mostly He that gather together in the core. To a lesser extent are synthesized by-products like Li and Be. During the He-phase is synthesized mostly C through the by-product Be and elements until O. The next big fusion process, the one of the C, synthesize O properly and further elements until Fe. Further fusion processes produce other elements to a lesser extent. Each fusion level release less energy than the previous one and run faster out. By Fe stops the fusion chain, since Fe has the highest binding energy and the fusion to heavier elements consumes energy instead of release it. The half of the elements beyond Fe is released to the ISM through the *r-process*, the nucleosynthesis that takes place in the outer shells of the Fe core during a SNII explosion. The other half is released by stellar winds during the AGB-phase.

The stellar yields represent the mass ejected from a star into the ISM, consisting of preexisting matter together with newly formed. Depending on the initial mass, the production of a certain amount of the different elements is expected according to the physical processes in stars of this mass. In Figure 1.2 is plotted the abundance number ratios to Fe in the cluster Abel 262. These values were fitted in Sato et al. (2009) by a combination of SNIa and SNII yields per supernova

to get the number of SNIa and the ratio SNII to SNIa. The SNIa yields were hereby better represented by the SNIa model W7 over the models WDD1 and WDD2. The ratio SNII to SNIa was estimated as 3 to 1, that means, only one fourth of all SN were SNIa. This result is similar for other clusters.
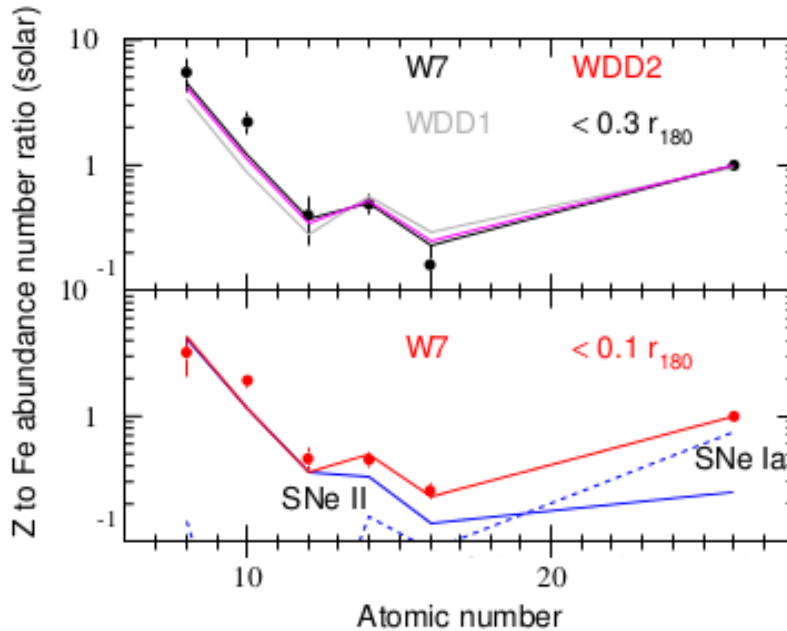
Figure 1.2: *Abundance number ratio of elements to Fe for the cluster Abel 262 in solar units (Sato et al., 2009). The top and the bottom panels show the fits for the abundances inside 0.27 r_{180} and 0.1 r_{180}, respectively. The red points show the values in the cluster, while the blue dashed and solid lines show the contribution of SNIa and SNII, respectively. For more information see Sato et al. (2009)*

One can infer from the fit in Figure 1.2 the contribution from each SN type to the observed abundance of each element as well. We can learn from these results, therefore, from which events the enrichment comes from. By looking at the distribution of the elements is possible to trace the events inside a cluster and its galaxies and gain a wider view about galaxy evolution and cluster evolution. In section 3 are treated the different metallicity gradients in clusters of galaxies.

1.1.2 Compact Objects

There are three classified compact objects: white dwarfs (WD), neutron stars (NS) and black holes (BH). The conditions under which a compact object becomes NS or BH remain unknown. They have following features, described briefly:

- Neutron star: They have extreme high densities of about 10^{11} to $2.5 \cdot 10^{12}$ kg/cm^3, the scale of atomic cores. They count with a diameter of only ~ 20 km and mass in the range of 1.4–3 M$_\odot$.

- Black hole: These compact objects are predicted in the general relativity as massive enough to deform spacetime. These objects exhibit such a big gravitational force that not even

photons can escape from their field. The threshold by which is not possible any more to escape is called the event horizon. Observationally appear as empty regions that produce enormous gravitational effects as gravitational lensing.

1.2 Evolution of Galaxies

1.2.1 Inside-Out Model

The disc of young galaxies grows, according to this model, from inside out through accretion of gas. The accreted gas towards the center triggers star formation (SF) when it is dense enough.

In Pastorello et al. (2014) is explained a two phases model. A first phase along $z > 2$ is called dissipative collapse. The SF at this stage is driven by the infall of cold gas or by cooling of hot gas. A second phase is called external accretion, by which usually old star populations are accreted. These propositions are in concordance with the observed negative metallicity gradients, usually steeper at large radii. Age and metallicity gradients show old metal rich stars in a metal rich environment in the inner region and young metal poor stars in a metal poor environment in the outer region.

This model is also supported by color gradients, SF history and a mass-size relation almost independent of the redshift. The proportionality between mass and radius depends just slightly on the virialization redshift, because systems that virialized first have larger mean initial densities, since the Universe was denser then (Chiosi et al., 2012).

1.2.2 Transition from Spiral- to Elliptical-Galaxies

Two clear trends for the stellar mass-metallicity relation (MZR) are recognized, the one of typical spiral, gas rich, star forming galaxies, and the one of typical elliptical, passive, quenching galaxies. In Figure 1.3 is shown the stellar MZR obtained from a big survey of all kind of galaxies, presented in Gallazzi et al. (2005), together with a differentiated plot of spirals and elliptical presented in Peng et al. (2015) from the same survey used by Gallazzi et al. (2005).

The difference of the slopes throw more lights in the transition from star forming- to quenching-galaxies, which seems to be part of the evolutionary process of all galaxies. In Figure 1.4 is illustrated the two possibilities for the transitions, explained in Peng et al. (2015). The first option is a slow gas loss caused by gas removal, due to tidal forces by approaching the center of a cluster. The second one is the so called *galaxy strangulation*, where galaxies keep forming stars until they run out of gas. This process is probably enhanced by starbursts produced in major merger events. There is almost never a collision between stars during a major merger, but the HII regions are agitated and trigger SF more rapidly than the usual rate. This galaxies are called then starbusts galaxies.

Elliptical galaxies show mostly higher stellar metallicities out of the slope of typical spiral galaxies, as can be seen in Figure 1.3, which supports an accelerated SF activity and the second scenario as the most common, or the most determinant, in the quenching process.
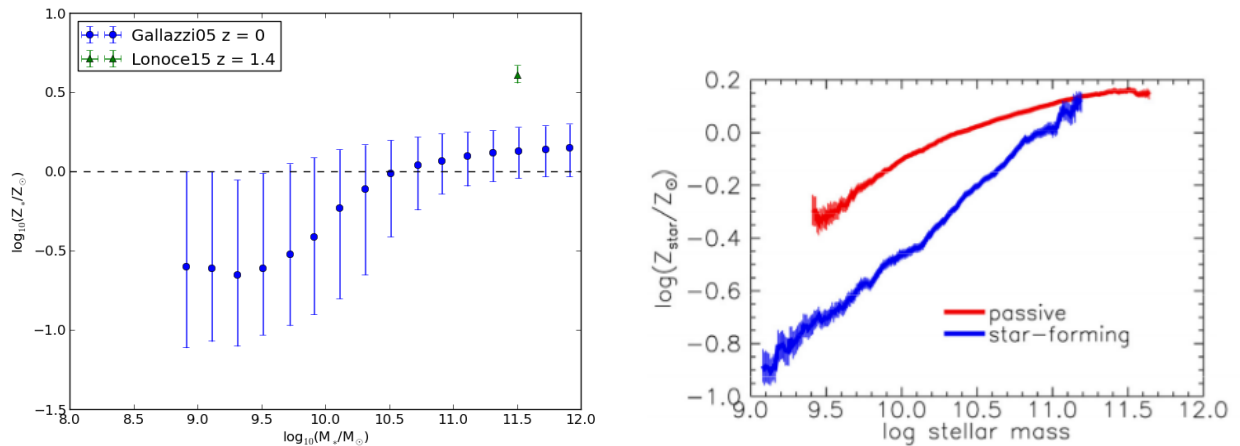
Figure 1.3: *Left: Stellar mass-metallicity Relation (MZR) as observed (Gallazzi et al., 2005). The big scatter is caused by the mixture of spiral and elliptical galaxies (star forming and quenching), which show different curves. Right: The different stellar MZR curves where star forming- and quenching-galaxies belong (Peng et al., 2015). As indicated in the graphic, in the top on red are placed the quenching passive galaxies and down on blue the star forming galaxies. Even a galaxy at redshift 1.4, a single galaxy measurement presented in Lonoce et al. (2015), which should be placed below the curve of Gallazzi et al. (2005) for being in a higher redshift, appears above, since it is a big elliptical, as can be seen in the left panel.*
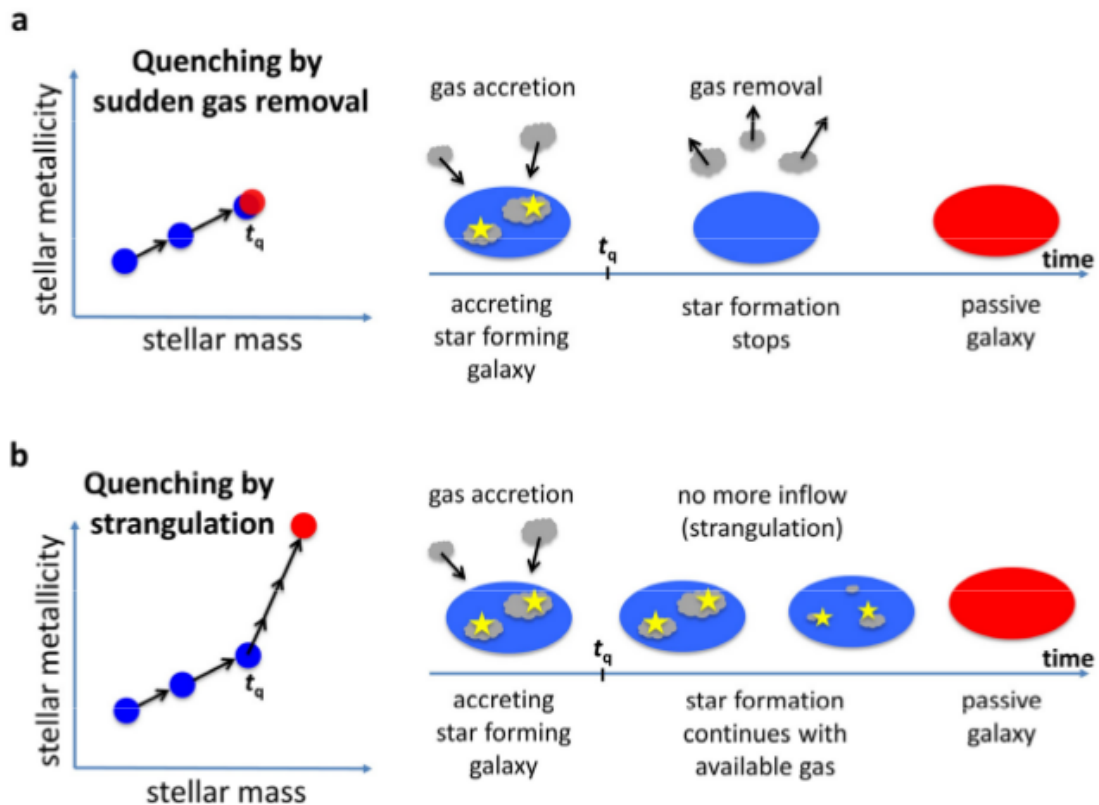
Figure 1.4: *Two models for the transition from star forming- to a quenching-galaxy, taken from Peng et al. (2015). a: Star formation (SF) stops by suffering gas removal. b: Galaxies keep forming stars until they run out of gas. This last SF activity is probably accelerated, evidenced in the higher stellar metallicities out of the slope of typical star forming galaxies, as illustrated in the MZR on the left side.*

2 Mass-Metallicity Relation

A strong correlation between the stellar mass and the metallicity, was first observed by Lequeux et al. (1979) for nearby irregular galaxies. Since there, many studies show similar results for every kind of galaxies out to z $\sim$ 3.

The mass-metallicity relation (MZR) shows the balance between gas inflow, the related star formation (SF) and gas outflow. Galactic outflows are observed to carry mass and metals to the IGM and they are produced principally by the composition of all the stellar winds within a galaxy and scale therefore with the star formation rate (SFR), but also with a fraction of the supernova (SN) energy that powers the wind.

Galactic outflows, however, depend not only on the own stellar activity of the galaxy, since as explained in more detail in Section 1.2.2, the gas can also be pulled off by tidal forces from a cluster. The SF self can be enhanced through a starbust produced by a big merger. The MZR doesn't represents a trivial relation that can be inferred from the physics of the stellar activity in a closed box model, but the result of a complex interplay that describes galaxy evolution globally.

The velocity of the galactic outflows scale with the escape velocity of the galaxy and also a bit with the dispersion velocity (Daveé et al., 2006). The mass-size relation ensures that the most massive galaxies are also bigger in general and retain more metals due to the stronger escape velocity and therefore less effective galactic wind. The galactic outflows seem of this way to be responsible for the slope of the MZR. Nevertheless, the nature of the MZR is not completely understood.

2.1 Gas-Phase Metallicity

Represents the metallicity of the ISM in gas-rich galaxies, namely in HII star forming (SF) regions, which are typically heated (around 10^4 K) and ionised by the big amounts of UV radiation from the SF activity. The O absorption lines are relative easy to observe from the spectrum of these nebulae, so is the O abundance used as reference for the metallicity in the gas.

The following expression is commonly used to describe the gas-phase metallicity:

$$12 + \log_{10}\left(\frac{O}{H}\right) \tag{2.1}$$

Where the ratio (O/H) represents the number ratio and not the mass ratio. This ratio, logarithmic, gives a slope suitable to analyse and compare. Using the semianalytical simulation FIRE, Ma et al. (2016) gives a linear approximation of the gas-phase metallicity, where the dependence on the redshift is included.

2.2 Stellar Metallicity

Represents the mean metallicity between all stars in the galaxy. While the gas-phase metallicity represents the actual highest metallicity level of the galaxy, the stellar metallicity represents a mean value through the time.

Although in some works is used a composition of several element abundances, the most extended definition for stellar metallicity is the following using the Fe content as reference, since for stellar spectra is convenient the observation of the Fe absorption lines:

$$\left[\frac{Fe}{H}\right] = \log_{10}\left(\frac{N_{Fe}}{N_H}\right)_{star} - \log_{10}\left(\frac{N_{Fe}}{N_H}\right)_{sun} \tag{2.2}$$

The correlation is stronger for galaxies between 10^9 M$_\odot$ and 10^{12} M$_\odot$. For less massive galaxies is shown a smaller and irregular star formation efficiency and so the chemical enrichment (Ma et al., 2016). An example of the stellar MZR can be seen in Figure 1.3 in Section 1.2.2, where is also shown the different behaviors for spiral- and elliptical-galaxies.

2.3 Evolution

Many independent works show an evolution in the MZR with redshift. Not surprising, a higher metallicity is observed by smaller redshift, showing how there is more metals produced with the pass of the time. Interesting is how the MZR seems to keep its shape, probing its universal meaning. The shape of the MZR is established probably around z $\sim$ 6 and remains constant after that, getting slowly just higher values, and flattening slightly its slope (Daveé et al., 2006).

Stars synthesize metals through the internal nuclear fusion processes during their evolution and galactic outflows are observed to carry these elements to the IGM (Daveé et al., 2006). These observations together with the insights acquired from gradients in clusters, explained in more detail in Section 3, throw away the possibility of a closed box model for the chemical evolution of galaxies. Some authors use the name *leaky-box model* because the apparently inevitable fate of the galaxies of finally losing their gas fuel.

Examples of the gas-phase MZR and its evolution can be seen in Section 4.3, where is described the related observational methods.

3 Metallicity Gradients

The distribution of the metals within a galaxy depends clearly on the mass of the galaxy. For the least massive Galaxies, around 10^6 $M_\odot$, the distribution is smooth, but dwarf lost almost all metals in the CGM and IGM. around 10^9 $M_\odot$ the most of the metals are already placed inside 10% of the virial radius R_{vir}, while for the most massive ones, around 10^{12} $M_\odot$, almost all of them are inside. This behavior is well reproduced in simulations, as reported in Ma et al. (2016) and consistent with the fact, that by smaller galaxies the metals can be spread out over a longer radius due to the smaller escape velocity of the galaxy. Galaxies heavier than 10^6 $M_\odot$ (Ma et al., 2016) instead, keep a big portion of the metals, since the galactic winds fail leaving the Galaxy and these metals are reaccreted.

3.1 Gradient in Galaxies

Early comparisons of metallicity gradients taking the absolute galactocentric distances showed any agreement between each other. It was realized that a common distance related to the physical properties of the galaxies should be chosen. The effective radius R_{eff} is shown to be a good normalization choice for the galactocentric distances.

3.1.1 Gas-Phase Gradients

In Figure 3.1 is evident the general decaying gradient for the O abundance. This tendency was analysed in Sánchez-Menguiano et al. (2016) to find dependencies with other galaxy properties like morphology, luminosity and the presence of bars. This slope seems to be independent on any other galaxy property but on the mass.

The mass classification in Figure 3.1 shows how the values of the metallicity go up, the more massive the galaxies are, as expected from the slope of the MZR, always maintaining the shape of the profile nearly equal. The special behaviors in the inner and outer regions start also in the same place in any case. Bigger than ~ 2 R_{eff} flatten out every of them, while lower than ~ 0.5 R_{eff} go down the most massive ones.

Active galaxy nuclei (AGN) are galaxies with a supermassive black hole (BH) in the center. AGN activity hinder the spectroscopy but also could push metals away from the center, if present. The inner region of the most massive bins flatten despite of the effort made in Sánchez-Menguiano et al. (2016) for excluding strong AGNs as well as weak AGNs. The nature of the flattenings in both, the inner and the outer region, remain a mystery.

Barred spiral galaxies are spiral galaxies with a central bar-shaped structure, usually called the
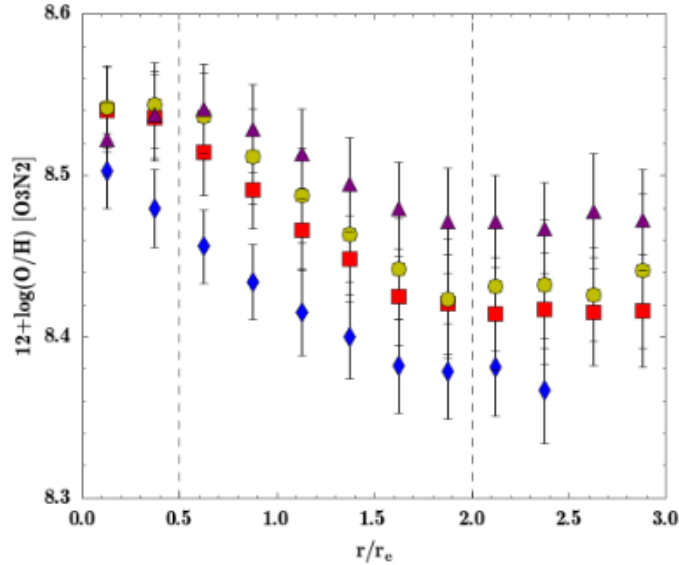
Figure 3.1: *Sánchez-Menguiano et al. (2016) present this radial profile of gas-phase metallicity gradient averaged from 122 face-on spiral galaxies from the CALIFA survey. The symbols represent the mean value and the bars the standard deviation. Four different mass bins were chosen in a way to ensure a comparable number of galaxies in each bin. Blue diamonds: $log(M/M_\odot) \leq 10.2$. Red squares: $10.2 < log(M/M_\odot) \leq 10.5$. Yellow circles: $10.5 < log(M/M_\odot) \leq 10.75$. Purple triangles: $10.75 < log(M/M_\odot)$. The dashed vertical lines separate the three different behaviors.*

bars, that concentrate ISM gas and stars. 30% - 40% of spiral galaxies have strong bars in the optical wavelength range and 60% if weak bars are considered (Sánchez-Menguiano et al., 2016). Some simulations predict that the presence of bars can produce this effect in the inner region due to the asymmetry they represent. Nevertheless, it was found no hint of such correlation according to Sánchez-Menguiano et al. (2016).

Some correlations were found in the past, only because the distances in each galaxy were expressed in absolute values and plotted together. In the most cases the correlations disappear after normalization to a representative distance. The R_{eff} seems to be the best choice so far, since it correlates with many other galaxy properties (Sánchez-Menguiano et al., 2016). For all further comparison with the results of the MAGNETICUM simulations in this work is used the R_{eff} to normalize the radial profiles.

Because of the technical difficulty, there are no numerous observations of gas gradients at higher redshifts. However, with new observational techniques is possible to build metallicity gradients until higher radii, about 8 R_{eff}, and at higher redshifts, about $z \sim 2$. At this redshifts some gas gradients are rather positive, indicating possibly cold accretion or mergers that happen at the moment, the latter being difficult to distinguish (La Barbera et al., 2012).

3.1.2 Stellar Gradients in Spiral Galaxies

There is lack of representation of one dimensional stellar metallicity gradients in spiral galaxies from available observational data. A comparison with the results of the MAGNETICUM simulations for the analysis, can be done therefore only for stellar gradients in elliptical galaxies. Figure
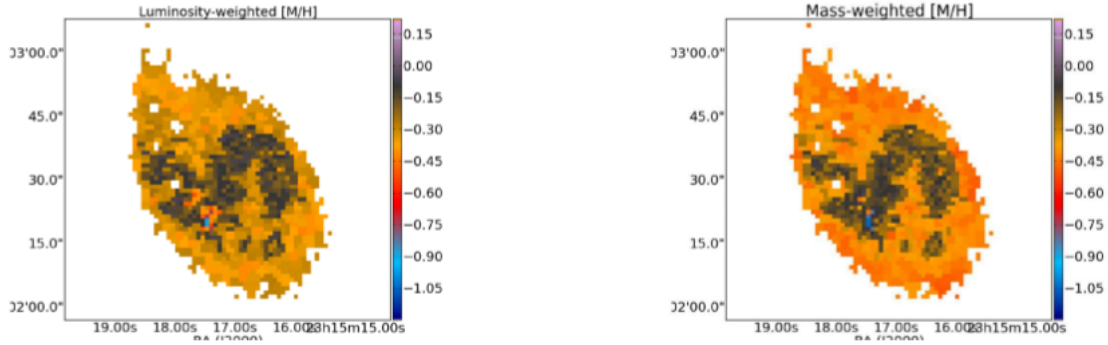
Figure 3.2: *Two dimensional stellar metallicity gradient of the spiral galaxy NGC 7549 from the CALIFA survey, luminosity-weighted on the left and mass-weighted on the right. Color coded is the stellar metallicity. Taken from Sánchez-Blázquez et al. (2014).*

3.2 shows a two dimensional gradient presented in Sánchez-Blázquez et al. (2014).

The flattening in the gas-phase metallicity seen in observations at higher radii is know to appear also by stellar metallicity gradients, suggesting an universal behavior.

As suggested in Sánchez-Menguiano et al. (2016), assuming the inside-out model, the stellar activity is not enough to produce the enrichment seen in the outskirts and it could be rather a consequence of minor mergers, disturbance of satellite galaxies or metal recycling. All these factors are not independent of each other and more information is needed to make a more accurate analysis.

3.1.3 Stellar Gradients in Elliptical Galaxies

The gradients of elliptical galaxies usually look more flat than the ones of spiral galaxies. This should reveal the origin of elliptical galaxies as the merger of two spiral galaxies, since from the merger follows the mixing of the content distribution. This scenario was confirmed several times in simulations. The metals produced by the stellar activity are the ashes of the evolutionary processes, in particular the observation of the stellar metallicity gradient, is the only true unequivocal proof of a merger event, not even the morphology.

While in-situ star formation (SF) and energy dissipation are the main processes to grow in early phases, accretion through minor mergers is seen in the later phases as the main origin of growing in size and shaping the metallicity gradients in massive galaxies at large radii.

At later phases, the accretion of old populations of metal poor stars is achieved without to influence the inner region of the galaxy. So is increased the R_{eff} and the Sersic index, which gives the radial profile of the surface brightness in single galaxies. A higher index indicates a higher luminosity in the center and a faster decay with the galactocentric distance.

Until 4 - 5 R_{eff} should be dominated by in-situ SF. From here on is still unclear if the stars were accreted or built in-situ, closer to the center, and then migrated to the outside. Insights about the latter would be key to understand the meaning of the AGN feedback. Massive galaxies by about 10^{13} M$_\odot$ are thought to have 40% till 60% of its stellar mass obtained by accretion, while smaller ones, without a big major event triggering starbust, until 95% (La Barbera et al., 2012).

After major mergers instead, the gradients flatten. In a major merger, two galaxies of comparable size merge and the dark matter of the system mix into the center through violent relaxation, i.e. a redistribution of the kinetic energy to reach thermic balance. The abundances mix hereby even at large radii (La Barbera et al., 2012).

Figure 3.3 shows mean gradients of elliptical galaxies separated in three mass regions. Despite of the irregularity in the lowest mass bin, the gradients shown to have in general higher values, the higher the mass is, as expected from the MZR. The shape of the gradients shows to be also independent of the mass and therefore universal.
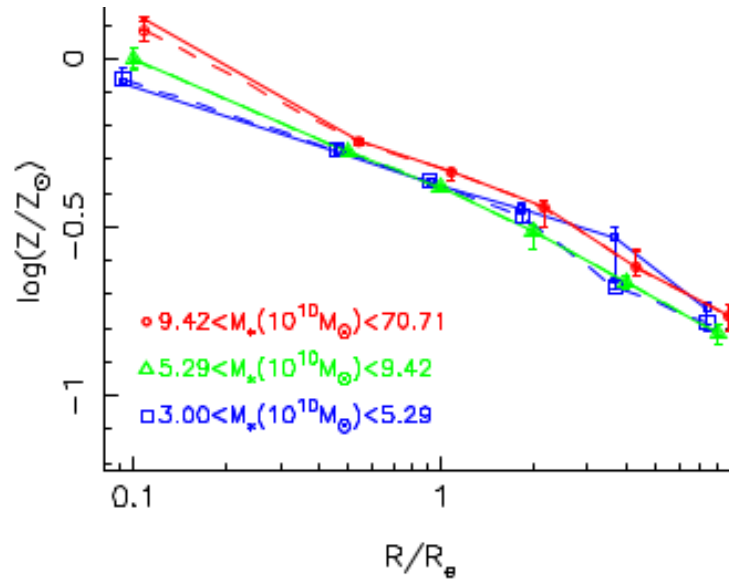
Figure 3.3: *Typical abundance radial profiles of stellar metallicity in elliptical galaxies, taken from La Barbera et al. (2012). The galactocentric distance is expressed logarithmic with the effective radius R_{eff} as unity.*

3.2 Gradients in Clusters of Galaxies

Figure 3.4 shows the gradients of different elements in the cluster Hydra A. Galaxy clusters with cold cores, like this one, show specially good spectral lines, as explained in more detail in Section 4.3. These gradients show, like in other clusters (lower panel in Figure 3.4), peaks of the elements in the center and a regular decaying behavior. Specially Fe shows a clear peak, suggesting a predominant SNIa enrichment in the central dominant galaxies, according to the different supernova (SN) yields shwon in Section 1.1.1. Nevertheless, the metal production in the central galaxies doesn't enrich automatically the ICM. It was already shown that AGN-ICM interaction play a determinant role in the transport of metals from the big central galaxies to the ICM (Simionescu et al., 2009).

From these gradients we can learn more about cluster evolution. The number of SNIa needed to reproduce the observed peaks of Fe, as well as the magnitude of stellar winds, are not enough to reproduce the observed peak of O. This suggests that there was a stronger SNII activity in the central region of the cluster in early phases, instead of a well mixed activity, as it was thought earlier (Simionescu et al., 2009).
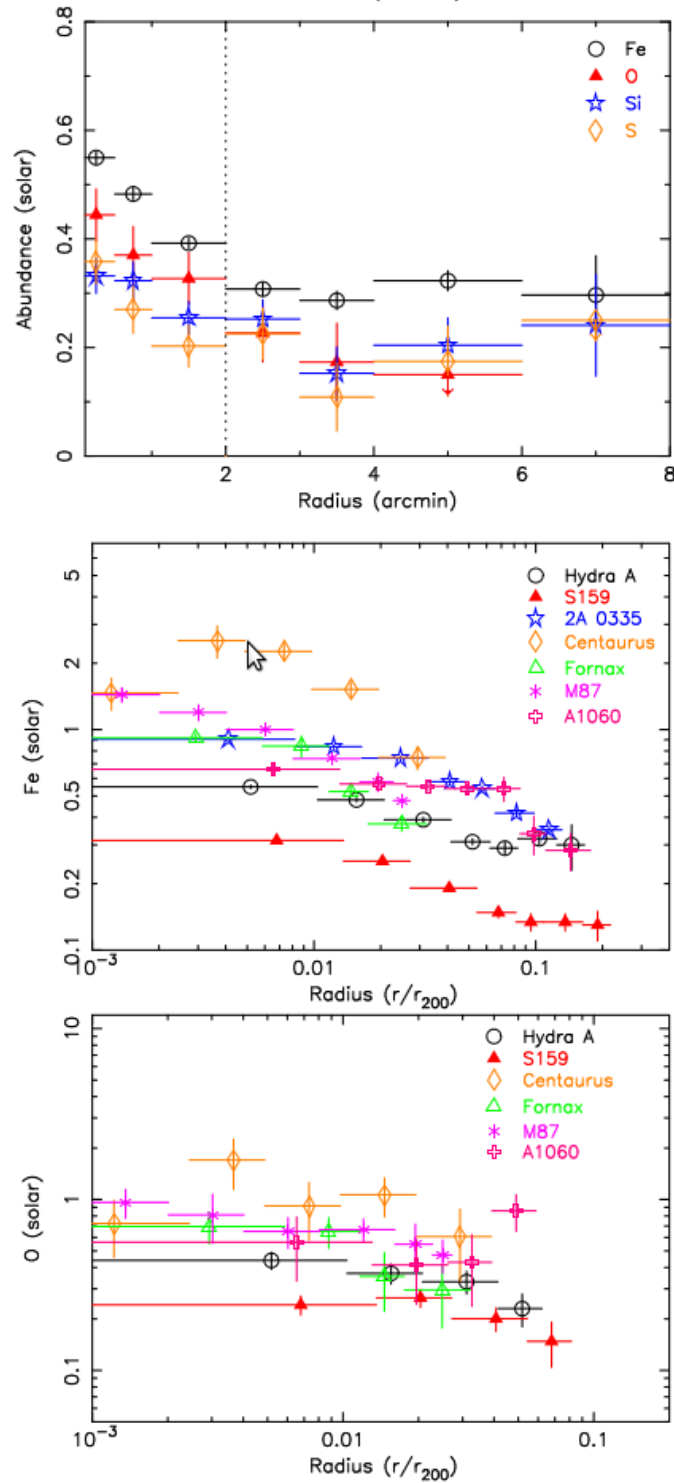
Figure 3.4: *Top: Abundance radial profiles of the four elements indicated in the graphic for the cluster of galaxies Hydra A. Taken from Simionescu et al. (2009). The vertical dashed line, where the behavior clearly changes, corresponds to the virial radius of the cluster. Middle and bottom: Comparison of the Fe and O profiles, respectively, with the other galaxy clusters indicated in the graphic. The radius is normalized to the virial radius of the cluster r_{200}.*

The gradients of Fe in Figure 3.4 are slight steeper than the ones of O. Sato et al. (2009) presents also gradients of many elements in the ICM in one selected cluster. Steep gradients are evident in all the studied elements, but in O, as can be seen in Figure 3.5. Even when there is a big uncertainty for O, the behavior is clearly more flat than for the other elements.
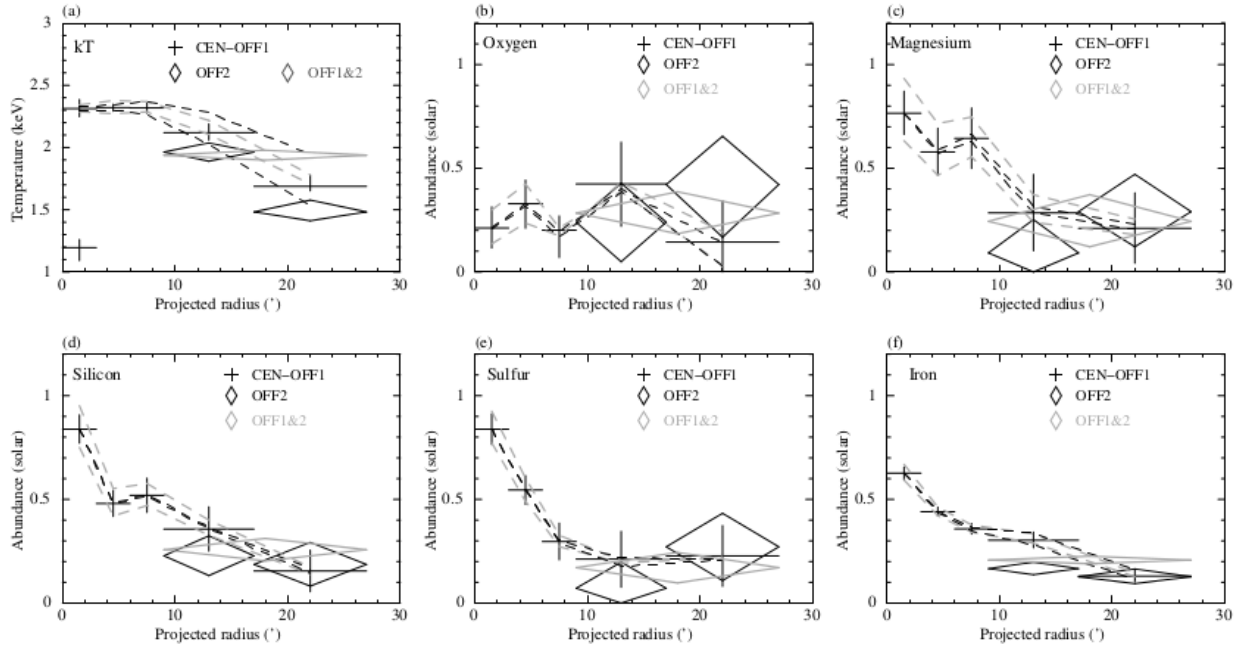
Figure 3.5: *In Panel a is shown a temperature radial profile in the ICM of the cluster Abel 262. The other panels show for these same region the abundance profiles of the indicated element in the panel, respectively. Taken from Sato et al. (2009)*

In Section 1.1.1 is shown how the SNIIs provide the most of the O to the environment (some is spread out by stellar winds), according with the actual SN models. Since this type of SN occurs more often than SNIa, about 3 to 1 today, the short living stars ending as SNII enrich the environment with huge amounts of O since the beginning of the stellar activity, so is not surprising that O is the most abundant metal in the universe.

The big amount of O produced in the galaxies, where star formation (SF) takes place, had a long time to be spread all over the cluster. SNIa in the other hand, is produced only after the long living stars hanged long time around until to capture some other star and start the typical process of a SNIa. Fe, which is typical produced by SNIa, enriched the environment therefore later and less.

This means also that the occurrence of SNIa in comparison to SNII increases considerably in the later stages of galaxy evolution, i.e. in elliptical galaxies with no more fuel to keep forming new stars and cause new SNIIs. At these stages, the galaxies find their way closer to the center of the cluster, making understandable a steeper gradient in the ICM than the one of O.

4 Observational Methods

Integral field spectroscopy (IFS) is a relative new observation technique that combines the spectrography with imaging techniques to reach a better space resolution for spectra. This technology offered in the last years analysis of wider HII regions, key regions for inferring metallicities. That is the case of the CALIFA survey, from which many of the observational data used in this work come from.

Is not the intention of this work to give a detailed description of the observational methods, nor to describe in detail the quantenmechanical concepts needed to follow some of them, but giving a view of the basics related to these, since the understanding of the conditions and limitations of the observations help to improve a more reasonable comparison with the data obtained from simulations. In the following there is a brief description of the measurement of mass and metallicity of gas and stars.

4.1 Gas Mass

In Santini et al. (2014) is explained how the mass of the gas is usually obtained from spectral emission lines from the dust in warm regions, in a process that systematically underestimate the total mass by $\sim 50\%$. In that work is presented the evolution of the star formation efficiency (SFE), in Figure 4.1, which is expressed as the star formation rate (SFR) divided by the enclosed gas mass. In this work was probed that the best fit with these observations are only achieved when the estimated gas mass from the simulations is reduced to the half to get artificially the reported error in the observational data.

4.2 Stellar Mass

The mass of a star can only be directly estimated from a binary system of stars. This mass is later used as a sample to estimate indirectly the mass of other stars with the same properties in the Hertzsprung-Russell diagram (HRD).

The mass-luminosity relation, showed below, is also a widely used tool to approximate the mass of stars and even the stellar mass of a galaxy.

$$\frac{L}{L_\odot} \approx= \frac{M}{M_\odot}^{3.5} \tag{4.1}$$

More precise methods have been developed to estimate the galactic stellar mass, than roughly using the mass-luminosity relation. The most used recipe in the last years has been the method
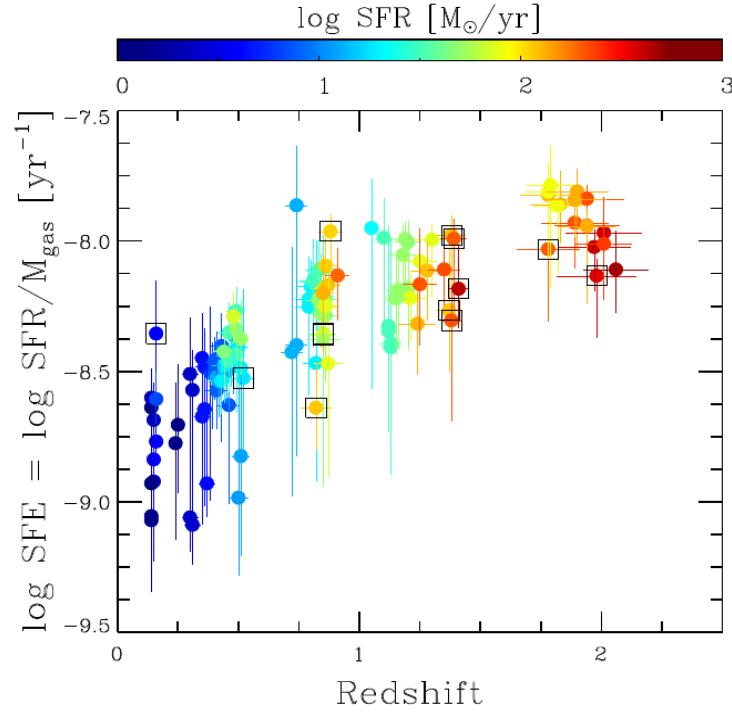
Figure 4.1: *Evolution of the star formation efficiency from z ∼ 2 until today, taken from Santini et al. (2014). Color coded appears the value of the star formation rate.*

BC03 (Bruzual and Charlot, 2003). To estimate the stellar mass of a galaxy, in general, is observed first the SFR in some mass region, usually bright young stars, and then the rest of stars formed with other initial masses are approximated with the initial mass function (IMF), which describes the distribution of initial masses in a population of stars.

4.3 Metallicity

The equivalent width of spectral lines, i.e. the surface with the same area as the line section, is used in astrophysical spectroscopy to measure the content of the element responsible for the interaction by estimating the number of interacting atoms.

The number of electrons able to absorb and scatter, however, depends on the temperature, since by high enough temperature the electrons can become ionised. To solve this issue is used the Saha ionisation equation, which describes the dependence on the temperature of the ionization level of a gas in thermodynamic equilibrium

$$\frac{n_{i+1} n_e}{n_i} = \frac{2}{\Lambda^3} \frac{g_{i+1}}{g_i} \exp\left[-\frac{\epsilon_{i+1} - \epsilon_i}{K_B T}\right] \tag{4.2}$$

Where n_i is the density of the atoms in the i-th level, n_e is the electron density, g_i is the degeneracy of states for the i-th level ions, ϵ_i is the energy required to remove electrons from the i-th level in a neutral atom and create an i-th level ion, K_B is the Boltzmann constant, T is the

temperature of the gas and Λ the thermal de Broglie wavelength of an electron:

$$\Lambda = \sqrt{\frac{h^2}{2\pi m_e K_B T}} \tag{4.3}$$

Where h is the Planck constant and m_e is the mass of an electron. AGN galaxies, however, are typical left from this analysis. For galaxies with AGN activity it is not feasible to infer the star formation rate (SFR) and metallicity from the spectral lines as usual, since the AGN activity affect the spectroscopy.

For the estimation of stellar metallicities are observed the absorption lines from the stellar atmospheres, while for the estimation of gas-phase metallicities are observed the emission lines in HII regions of gas rich galaxies. These regions are typically heated ($\sim 10^4$ K) and ionised by the action of the stellar activity and nearby supernovae.

Stellar metallicity measurements are more accurate and free of typical systematic errors observing galactic nebulae. The limitation is the distance at which the spectroscopy for single stars can be done. In general there is only available observations of stellar metallicity in the local universe. Lonoce et al. (2015) offers a estimation of the stellar metallicity of a single big elliptical galaxy at redshift 1.4.

The age of the stars can be estimated at the same time with stellar spectroscopy, among many other methods. The Fe content in stars play a key role in this concern, since it is abundant and relatively easy to observe, and a star without Fe was surely born in an early stage of the universe, where the environment was still not enriched with Fe. So is the Fe content commonly used as an indicator of the age of stars.

For the estimation of gas-phase metallicity in low mass galaxies is possible a direct measurement of the abundances in the ISM. For massive galaxies instead, is needed some calibration. These calibrations use an empirical, theoretical or hybrid relation between observed ratios of strong emission lines in nebulae close to star forming regions, and the abundances of the elements responsible for the emissions. In the last years, however, a new method that infers the gas-phase metallicity out of the metallicity of the youngest stars seems to overcome the problems of earlier measurements, at least in the local universe, where stellar measurements are possible. All these methods are described in the following sections.

4.3.1 Direct Method

This is the only truly trustable method inferring metallicity from galactic nebulae. Spectroscopy of the temperature-sensitive [OIII] α_4363 line is used to infer the O content in nebulae directly from the temperature of the electrons. This method is therefore also called the T_e method. These lines are specially weak in massive, metal-rich objects and their detection in individual galaxies is in general only possible in the low mass end of the MZR, i.e. for galaxies in the stellar mass range of $\log(M/M_\odot) \sim 7.4$-8.9 (Andrews and Martini, 2013).

Andrews and Martini (2013) used stacked spectra of ~ 200000 star-forming galaxies to enable the detection of these temperature-sensitive lines in more massive galaxies and expand the direct

method to $\log(M/M_\odot) \sim 10.5$. In Figure 4.2 is shown a comparison of different strong-line calibrations with the expanded direct method.
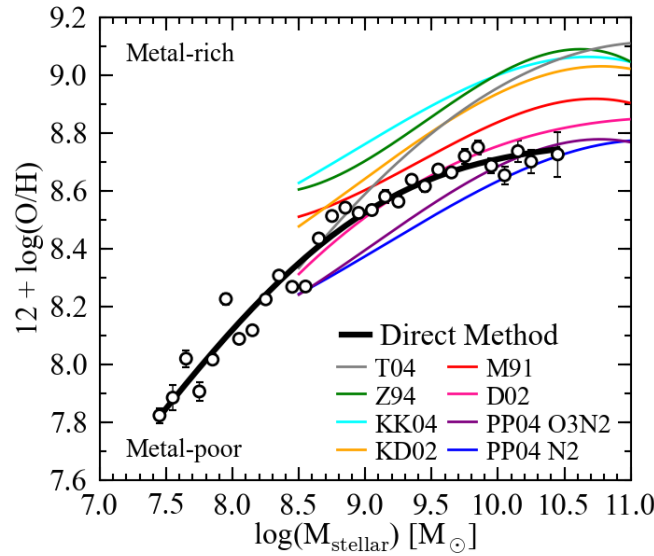
Figure 4.2: *Circles and black line show the result of the direct method of gas-phase metallicity estimation presented in Andrews and Martini (2013), for which the high mass limit is expanded from $\log(M/M_\odot) \sim 8.9$ to $\log(M/M_\odot) \sim 10.5$ by stacking the spectra of ~ 200000 star-forming galaxies. In color is shown different calibrations made with strong-line methods.*

4.3.2 Strong-Line Analysis

The strongest spectral lines can be observed from the Earth and space until $z \sim 3$. The most accurate methods to infer the metallicity in the gas, however, require the weak lines. Over $z \sim 0.2$ is used exclusively strong-line methods. With these methods are observed the emission lines from warm ionised HII regions within star forming galaxies and the results are calibrated through T_e-based metallicities in the local universe.

These methods represent a process full of difficulties and systematic errors. In general is difficult to get absorption lines from warm gas, since from one specific temperature up, the atoms collide to each other in such a way that they become ionised and not longer suitable to absorb new energy through their electrons (Simionescu et al., 2009).

Figure 4.3 shows a comparison of many different calibrations, each one apparently more appropriate for mitigating problems related to observation conditions in different situations, like the observed band, the absorption and even the redshift. The graphic shows a strong discrepancy between one method and another in slope, absolute values and even the dispersion along the mass range.

Knowing the discrepancies between calibrations, the comparison of gas-phase metallicities at different redshifts may only be done between same calibrations. If no observation with a specific calibration is available at some redshift, then is necessary to make a correction first. In Kewley and Ellison (2008), Maiolino et al. (2008) and other works are given transformations between calibrations based on empirical relations. Only of this way is possible an analysis of evolution.
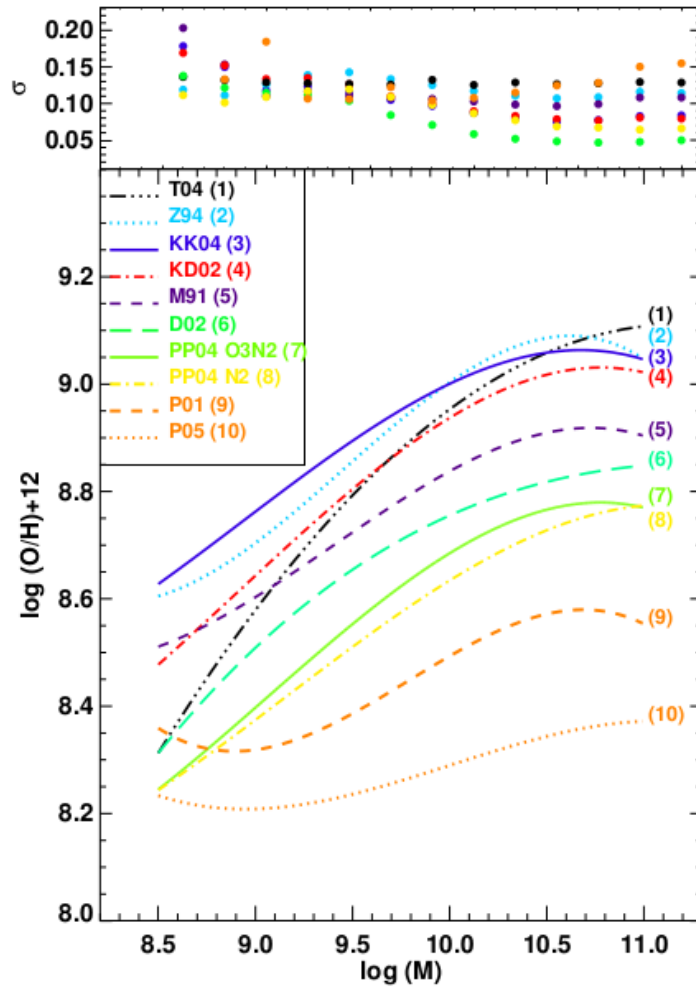
Figure 4.3: *In this graphic presented in Kewley and Ellison (2008) is perfectly seen the significant discrepancy in values and slope for a bunch of the widely used strong-line calibrations for estimating the gas-phase metallicity. In the upper frame is shown how even the scatter vary along the mass range in a different way for the different calibrations.*

Nevertheless, these procedure don't erase the discouraging feeling, by looking at Figure 4.3, that probably none of these calibrations is close to the reality anyway. As Kewley and Ellison (2008) points out, the temperature fluctuations or gradients in th HII regions may cause wrong estimations of the electron temperature, from which is inferred the level of ionisation (see Equation 4.2), key to estimate the chemical content.

Even using always the same calibration, there might be discrepancies at different redshifts. The comparison at different redshifts is just accurate if none of the involved physical properties evolve in time, like the gas density, ionisation, N/O ratio, among others, since they are assumed to be constant by the calibration. Many of these properties are already probed to evolve. As pointed out in Maiolino et al. (2008), one of the main worries using these observational methods based in strong emission lines, is that the dependence of these lines on metallicity involves also other dependences and the evolution of these galaxy properties with redshift may easily affect the validity of the locally made calibrations, at higher redshifts. However, in Maiolino et al. (2008) is also presented a test that show how the deviation in the calibration between local galaxies and high redshift galaxies is only faint, about 0.1 dex. dex(x) represents one order of magnitude in $\log_{10}(x)$.

4.3.3 Young Stellar Metallicity Method

In Bresolin et al. (2016) is proposed a method based on the stellar metallicity of spiral galaxies to estimate the gas-phase metallicity. Of this way, the estimation is independent of the numerous systematic uncertainties related to the typical strong-line analysis by observing nebular emissions, which finally produce important deviations along the wide mass range and eventually discrepancies between different calibrations.

In that work were selected a bunch of blue supergiants at different radii from the galaxy M83 to measure their metallicity. The metallicity of giant stars represent the closest value to the metallicity of the surrounding gas, since they are relative young. The stellar metallicity obtained from these stars, represents thus the mean value in one of the latest snapshots in the evolution of the galaxy. This value is then corrected to represent the oxygen content of the gas at the time these stars were born. In Figure 4.4 are these galaxies plotted and compared with typical results with some strong-line calibrations.
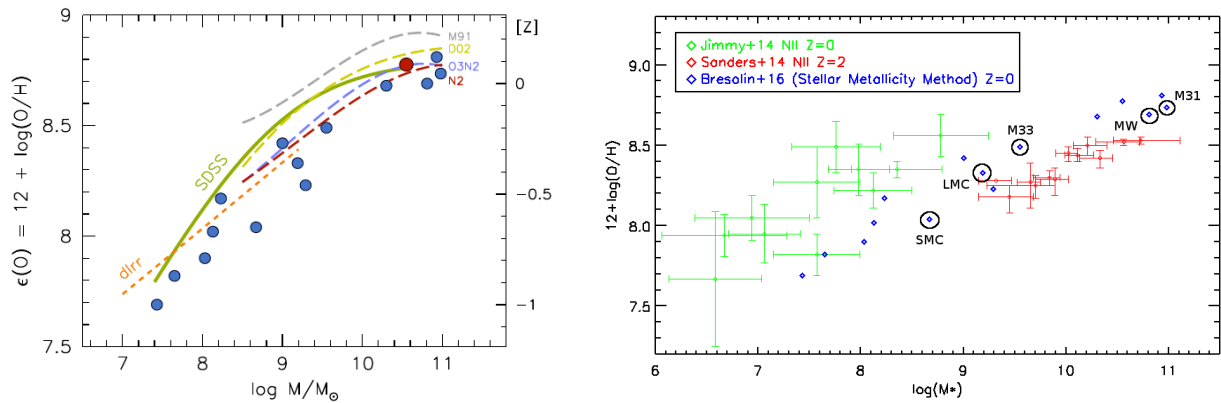
Figure 4.4: *Left: The blue points represent the gas-phase metallicity of 15 star-forming galaxies determined from the stellar metallicity of blue supergiant stars. The red point belongs to the M83 galaxy, the object of study in Bresolin et al. (2016), where this picture was taken from. The dashed lines correspond to the strong-line calibrations that fit the best this method. These can be compared with others in Figure 4.3. Their values lie about in the middle of the other widely used calibrations. Right: A direct comparison with independent observations using the NII calibraton at redshift 2 and 0. As predicted in the left panel, the NII calibration seems to be trustable for massive galaxies, but still overestimates the metallicities in the low mass end.*

The left axis in the left panel in Figure 4.4 shows the gas-phase metallicity and the right one the stellar metallicity. The correction is made using the O abundance in the sun. Denoted as $\epsilon(0)$, the typical expression used to describe the O abundance in galaxies, $12 + \log(O/H)$, for the sun, is thought to be 8.69 (Bresolin et al., 2016). Since the stellar metallicity is expressed in solar units and also logarithmic, the stellar metallicity of the sun should be zero. For the sun thus, the both axis should be shifted, so that the 0 in the stellar metallicity lies at the same height as the 8.69 in the gas-phase metallicity. Using this method, therefore, the stellar metallicity of spiral galaxies, inferred from blue giant spectroscopy, should be simply shifted 8.69 in the positive direction to get the corresponding gas-phase metallicity.

Bresolin et al. (2016) show how among the strong-line methods, the hybrid calibrations, a combination of theoretical calibration in the high mass end and empirical in the low mass end, produced the best agreement with the profiles obtained from stellar metallicities. Consequently, in this work

are preferred the comparisons with observations of metallicity estimated with these methods in the last years.

The hybrid methods, namely the NII and O3N2 calibrations in Figure 4.3, corresponds to the following strong-line ratios:

- NII: $\frac{[NII]}{H\alpha}$

- O3N2: $\frac{[OIII]\alpha5007}{H\beta} \cdot \frac{H\alpha}{[NII]\alpha6584}$

For making these calibration is used the measurement of extragalactic HII regions, where it is able to measure the abundance directly, and additionally the measurement of nebulae where the O abundance can be inferred from photoionisation models that relate this ratio with the abundance. Then the model is fitted with the empirical data at high metallicities (Bresolin et al., 2016). These methods are described in detail in Denicoló et al. (2002) (D02) and Pettini and Pagel (2004) (PP04), respectively.

4.4 Galactocentric Distances

Where is the end of a galaxy is not an easy question, since the mass of the galaxies spread over a big and diffuse range. A widely used concept in astronomy to define a representative galactocentric distance is the virial radius R_{vir}, within which virial equilibrium holds, that is, the virial theorem in equation 4.4, holds. T represent the total kinetic energy of the system and V the total potential energy. The brackets represent an average over time.

$$2 <T> = - <V>$$

(4.4)

At this radius the surrounding mass is considered bounded enough to the system. The mass inside this radius is called therefore virial mass M_{vir}.

Observationally, is difficult to determine R_{vir}. In cosmology is often used an approximation as the radius, within the mean density is greater than the critical density, in equation 4.5, by some factor. Here is H the Hubble constant and G the gravitational constant.

$$\rho_{crit} = \frac{3H^2}{8\pi G}$$

(4.5)

Simulations show that about 200 this factor correspond to R_{vir}. So R_{vir} is often represented as r_{200} as well. A similar notation is often used to indicate other distances to the center of a galaxy or a cluster of galaxies and keep no relation to R_{vir}. So is the $R_{1/2}$ radius at which the half of the total integrated luminosity in the K_s-Band is contained, also known as the effective radius R_{eff}. The radius R_{25}, on the other hand, represents the radius at which is placed the 25th mag/arcsec^2 isophote in the B-Band. The R_{vir} of the Milky Way comes curiously to ~ 200 kpc.

5 Simulating Chemical Enrichment

Cosmological hydrodynamical simulations use enriched galactic outflow to compare predictions in the mass-metallicity relation (MZR). Reproducing this enrichment requires a detailed simulation of the relevant feedback processes during the stellar evolution. In the following, we review in more detail each step of the stellar evolution, the feedback processes and the related decisions made for the enrichment model of Tornatore et al. (2007) and specially in the implementation for the MAGNETICUM simulations.

In comparison to previous works simulating chemical evolution, in Tornatore et al. (2007) is: studied the effect of changing the initial mass function (IMF) according to the local conditions and over time, included the life time of stars of different masses, studied the effect of changing the feedback efficiency and the different schemes to distribute SN ejections over star-forming regions and followed the production of single elements, instead of a global metallicity.

5.1 Star Formation

In hydrodynamical simulations, star particles are formed in dense regions of gas particles and represent populations of stars with the same age and initial metallicity. The number of stars that can be represented per particle is so small as the resolution level permits. The used model of SF in this work is the SH03 model described in Springel and Hernquist (2003), in which gas exists in three phases:

1. Hot gas cools via radiative cooling.

2. Cold clouds form stars at a rate given by the Kennicutt-Schmidt law. That means in the simulation that gas particles start to be treated as multiphase by reaching a threshold density.

3. Stars explode and restore hereby mass and energy to the environment. Hence, star- and gas-particles can have variable masses due to the mass transfer from a star with mass loss to the surrounding gas particles. With the energy, the surrounding gas particles become momentum and are heated with an efficiency that scales with the gas density.

The Kennicutt-Schmidt Law is an empirical relation between gas density and star formation rate (SFR). The SFR surface density Σ_{SFR} is proposed to scale with the gas surface density Σ_{gas} with as a positive power law with some positive power n.

$$\Sigma_{SFR} \propto (\Sigma_{gas})^n \tag{5.1}$$

Σ_{SFR} is usually expressed in units of solar masses per year per square parsec and Σ_{gas} in grams per square parsec. It has been suggested a value of n between 1 and 3.

Semi-analytical Models (SAM) are a widely used tool in the last years. They use first normal merger trees, and afterwards is added the result of analytical models that describe the physical processes of interest in the development of the n-body system. SAMs have a lower computational cost than hydrodynamical simulations and are capable to reproduce many features of galaxies (Ma et al., 2016).

Hydrodynamical simulations are powerful reproducing statistical properties of galaxies but they use a poor mass- and space-resolution, so is not possible to point out where and when exactly star formation (SF) happens. Empirical models are used to simulate SF, how the stellar winds are expelled and how they interact with the environment. At the end, the same problems as for SAMs with smaller masses are present. Like SAMs, they use inaccurate models for SF and stellar feedbacks and produce different evolutions of the MZR (Ma et al., 2016).

A challenge for SAMs is to achieve a good reproduction of the observed star formation rate (SFR), mass and metallicity at the same time. This goal is usually achieved by z = 0 but failed by higher redshifts, especially in the low-mass edge. The newest SAMs achieve to reconcile the masses with the SFR and even the color by z = 0-3, but metallicity remains a challenge (Ma et al., 2016).

5.2 Initial Mass Function

The initial mass represents the mass, the star entered the main sequence with, which is essential to determine the evolution path of stars. The initial mass function (IMF) describes the distribution of initial masses in a population of stars, that is, how many stars per mass range have a initial mass in this range. The IMF is therefore widely used in simulations, since they commonly treat stars statistically as groups.

It is still not clear, whether the IMF is universal or dependent on the environment, i.e. dependent on the local temperature, pressure and metallicity, or whether it is time dependent (Borgani et al., 2008). In simulations is assumed to be invariant.

The shape of the IMF determines the ratio between long-living- and short-living-stars, which defines the ratio between supernovae type II and type Ia (SNII and SNIa) and the related abundances. IMFs that provide a large number of massive stars are usually called *top-heavy*. The first and most simple used representation for massive stars was described by Edwin Salpeter

$$\phi(m) \propto m^{-1.35} \tag{5.2}$$

The Salpeter IMF is reported in Tornatore et al. (2007) to reproduce observed Fe gradients. Many observations, however, favor a multi-slope IMF with a flattening in the low-mass edge. In the MAGNETICUM simulations is preferred the Chabrier IMF, which is characterized by a mild larger number of massive stars, with the corresponding smaller number of low mass stars

$$\phi(m) \propto \begin{cases} m^{-1.3} & m > 1M_\odot \\ e^{\frac{-(\log(m)-\log(m_c))^2}{2\,\sigma^2}} & m \leq 1M_\odot \end{cases} \tag{5.3}$$

Figure 5.1 shows a comparison between the Salpeter IMF, the Kroupa- and the Chabrier-IMF. In the right panel is seen how the Kroupa IMF, in comparison to the Salpeter IMF, underestimates low mass stars as well as very high mass stars. The Chabrier IMF instead, correct the number of low mass stars but without to underestimate high mass stars. In the left panel can be appreciated even better how starting in ~ 2 $M_\odot$ the Kroupa IMF underestimates strongly the number of stars in comparison to the Salpeter IMF, while the Chabrier IMF remains nearly equal, with slight higher values.
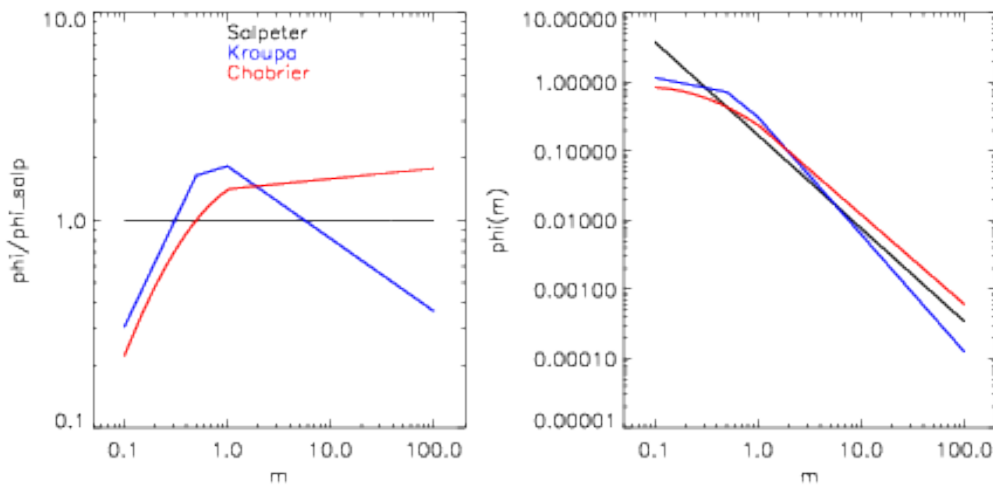
Figure 5.1: *Comparison between the two indicated mild heavier IMFs in the graphic with the Salpeter IMF in a logarithmic mass range within 0.1 $M_\odot$ and 100 $M_\odot$. Left: The ratio relative to the Salpeter IMF. Right: the absolute IMF in each case.*

To illustrate the effect of the IMF in the metal distribution, Figure 5.2 shows a comparison of three IMF choices presented in Tornatore et al. (2007) for a galaxy cluster: The Salpeter IMF, a top-heavy IMF and the mild heavier Kroupa IMF, similar to the Chabrier IMF used in the MAGNETICUM simulations.

All three cases in Figure 5.2 show an excess of enrichment in the central virial region of the cluster, as expected from the discussion in Section 3.2. In the right panels can be seen how the SNII contribution to the global metallicity concentrates in the high density regions, while the contribution of SNIa and AGB have more impact in the diffuse medium, as predicted in the cluster gradients shown in Section 3.2.

In the left panels in Figure 5.2, the top-heavy IMF shows clearly less Fe enrichment with a clumpier distribution in the gas in comparison to the other two functions, probably for not being enough for a proper distribution. In the right panels, in the other hand, is evident a higher SNII contribution from the top-heavy IMF. In comparison to the Salpeter IMF, the Kroupa IMF shows only a slight lower SNII contribution, apparently needed to reach better agreements with the observed abundances.
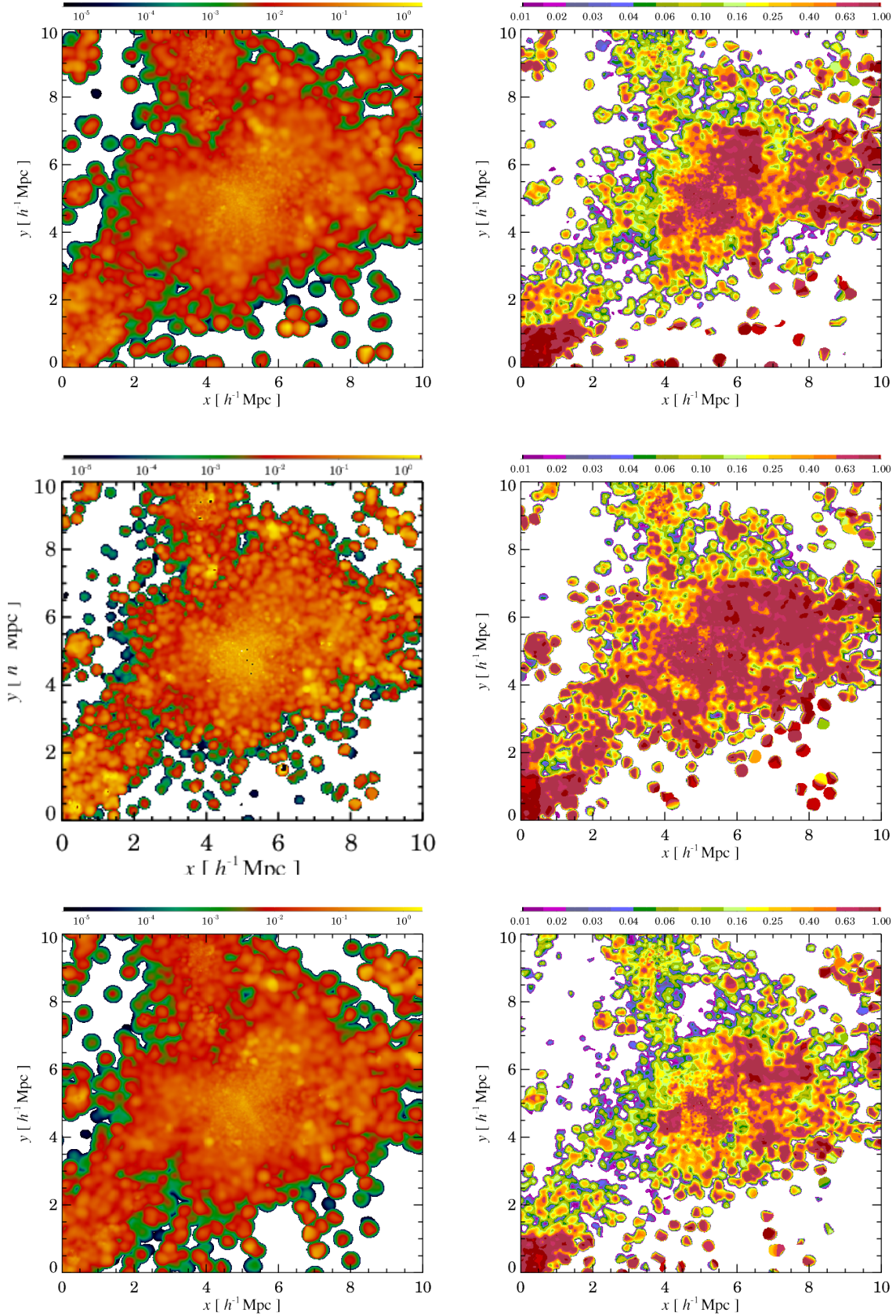
Figure 5.2: *Maps of metallicity for the enrichment model of (Tornatore et al., 2007) with three different IMF choices in a cluster within the box with the indicated size. Top: Salpeter (1955) IMF. Middle: The top-heavy AY IMF (Arimoto & Yoshii 1987). Bottom: The Kroupa (2001) IMF, similar to the Chabrier one. Color coded appears the gas-phase metallicity. The left panels represent the Fe abundance and the right ones the contribution of the SNII products to the global metallicity.*

5.3 Lifetime Function

The lifetime function defines the age at which a star of mass m dies. With the improvement of taking in account the lifetime of stars, the stellar feedbacks are reproduced more realistic by accounting with the time delay between star formation and the release of energy and metals.

The choice of the lifetime functions influence directly the absolute and relative abundances, by means of the different number of supernovae events of each kind.

In the MAGNETICUM simulations is used the lifetime function proposed by Padovani & Matteucci (1993) (PM03)

$$\tau(m) = \begin{cases} 10^{[(1.34-\sqrt{1.79-0.22(7.76-\log_{10}(m)))}/0.11]-9} & m \leq 6.6\,M_\odot \\ 1.2\,m^{-1.85} + 0.003 & \text{otherwise} \end{cases} \tag{5.4}$$

The lifetime function is assumed to be independent of the metallicity, although this dependence could be included.

Figure 5.3 illustrates different choices of lifetime functions in comparison to the PM03. The PM03 fits the value of 10^9 years for 1 $M_\odot$, the theoretical lifetime of the sun, and shows in general lower lifetimes in the whole mass range, but in the under-solar region, where some other functions underestimate the predictions.
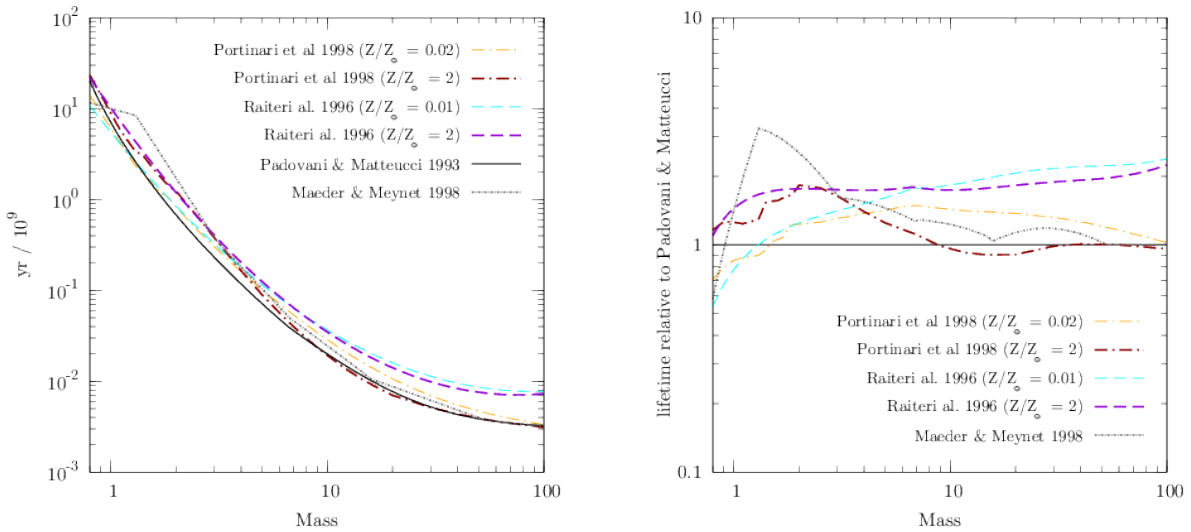
Figure 5.3: *Comparison between the different lifetime functions indicated in the graphic, taken from Borgani et al. (2008). Left: simple mass dependence of the different lifetime functions. Right: Mass dependence of the ratio relative to the PM03 (black line).*

5.4 Stellar Yields

The stellar yields $p_{Z_i}(m,Z)$ are defined as the mass of the element i produced by a star of mass m and initial metallicity Z at the end of its evolution.

As can be seen, the dependence of the yields on the initial metallicity is included, but only on the total metallicity. For element i, however, the specific metallicity Z_i plays a role. Solar abundances are assumed again to represent a good approximation for the mean behavior in cosmological scales.

To illustrate the impact of the selected yields, Figure 5.4 shows a mass ratio, for a group of common simulated elements, between two different sets of stellar yields. The ratio varies dramatically for different initial metallicities.
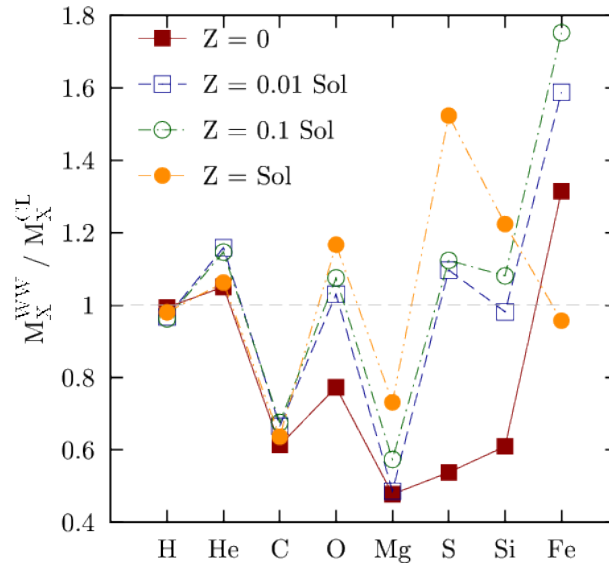
Figure 5.4: *Mass ratio for each indicated element in the graphic between the sets of yields proposed by Woosley & Weaver (1995) and by Chieffi & Limongi (2004), WW and CL, respectively, with the four indicated initial metallicities. Taken from Tornatore et al. (2007).*

In the set of simulations tested in this work were used the set of yields from Woosley & Weaver (1995) for SNII, Thielemann (2003) for SNIa and Amanda Karakas (2007) for AGB-winds.

5.5 Enrichment

The enrichment is calculated whether through the contribution of supernovae type II (SNII), supernovae type Ia (SNIa) or AGB-winds. SNIa and SNII contribute with energy feedback, while these two, together with AGB-winds, contribute with the chemical enrichment. The decisions made on the initial mass function (IMF), the lifetime function and the stellar yields define the accuracy of these contributions and of the enrichment model itself.

The metal release by stars is estimated as follows: The number of stars in each mass region (SNII, SNIa or AGB) is calculated integrating the IMF over the corresponding region, multiplied by the mass of the stars. Multiplying the latter by the corresponding stellar yield results in the whole released mass of the element i. Since only the dying stars contribute with the metal release at some time t, the mass contributions are constrained by the lifetime function. The following

generic formulation is exposed in Borgani et al. (2008)

$$
\dot{\rho}_i(t) \;=\; -\psi(t) Z_i(t)
$$

$$
+\; A \int_{M_{\mathrm{Bm}}}^{M_{\mathrm{BM}}} \phi(m) \left[\int_{\mu_m}^{\mu_M} f(\mu)\psi(t-\tau_{m_2}) p_{Z_i}(m,Z)\,\mathrm{d}\mu \right] \mathrm{d}m
$$

$$
+\; (1-A) \int_{M_{\mathrm{Bm}}}^{M_{\mathrm{BM}}} \psi(t-\tau(m)) p_{Z_i}(m,Z)\phi(m)\,\mathrm{d}m \tag{5.5}
$$

$$
+\; \int_{M_{\mathrm{L}}}^{M_{\mathrm{Bm}}} \psi(t-\tau(m)) p_{Z_i}(m,Z)\phi(m)\,\mathrm{d}m
$$

$$
+\; \int_{M_{\mathrm{BM}}}^{M_{\mathrm{U}}} \psi(t-\tau(m)) p_{Z_i}(m,Z)\phi(m)\,\mathrm{d}m
$$

M_{U} and M_{L} represent the upper and lower stellar mass limit taken in account in the model, respectively. Typical values are $M_{\mathrm{U}} \sim 100\ M_{\odot}$ and $M_{\mathrm{L}} \sim 0.1\ M_{\odot}$. M_{BM} and M_{Bm} represent the maximum and minimum allowed stellar mass for binary systems, respectively. These are typically defined to be $M_{\mathrm{BM}} = 16\ M_{\odot}$ and $M_{\mathrm{Bm}} = 3\ M_{\odot}$.

$\dot{\rho}_i(t)$ represents the evolution of the mass for the element i at the time t. $\psi(t)$ represents a generic form of the star formation rate (SFR) and $Z_i(t)$ the abundance of the element i, both at the time t. The first line in Equation 5.5 describes therefore the total lost of mass of element i by means of being locked in new built stars.

$\phi(m)$ is the value of the IMF with mass m, $p_{Z_i}(m,Z)$ is the stellar yield of the element i for stars with mass m and initial metallicity Z. ψ in the rest of lines in Equation 5.5 represents only the mass of the dying stars according to the lifetime function $\tau(m)$, that is, the stars built in the first $t-\tau(m)$ moments. Multiplying all these elements and integrating over the corresponding mass region results, as explained above, in the total released mass from the dying stars.

The second line in Equation 5.5 corresponds to the mass region of SNIa. The constant A denotes the fraction of stars in binary systems that can be progenitors of SNIa. In this model, this fraction is assumed to be constant A = 0.1, since it was found that with this value the Fe enrichment was well reproduced (Borgani et al., 2008).

The third line corresponds to the contribution of AGB stars, which in this model are considered as the rest of stars from the SNIa mass region that are not progenitors of SNIa, i.e. the (A-1) fraction of them.

The fourth line corresponds to the mass region of intermediate and low mass stars (ILMS) and the last line corresponds to the SNII region.

The SNIa contribution in the second line of Equation 5.5 has the peculiarity that not every combination of masses are considered possible in a potential SNIa binary system. The amount of stars is therefore multiplied by a fraction representing all the possible combinations of masses. μ represents the fraction m_2/m_B, where m_2 is the mass of the companion in the binary system and m_B the total mass of the system. μ is distributed according to $f(\mu)$ and the limits are set to

$\mu_m = \max[m_2(t)/m_B,\ (m_B - 0.5\ M_{BM})/m_B]$ and $\mu_M = 0.5$.

The metal releases are also multiplied by a time rate, proper of each event and dependent on the mass of the dying stars, and then multiplied by the time step, producing a more realistic delay in the enrichment. The SNII time rate, which also holds for ILMS, is obtained by simply multiplying the IMF by the stellar mass change rate, which is obtained convoluting the lifetime function with the SFR.

$$R_{SN\,II|ILMS}(t) = \phi(m(t)) \times \left(-\frac{\mathrm{d}\,m(t)}{\mathrm{d}\,t}\right) \tag{5.6}$$

For the SNIa time rate is used instead the same considerations made in Equation 5.5

$$R_{SN\,Ia}(t) = A \int_{M_{Bm}}^{M_{BM}} \phi(m_B) \int_{\mu_m}^{\mu_M} f(\mu)\,\psi(t - \tau_{m_2})\,\mathrm{d}\mu\,\mathrm{d}m_B \tag{5.7}$$

In the original model of Tornatore et al. (2007), only a percentage of SNe of each type is fixed to explode. 10% of SNII and 2% of SNIa. This delay in the explosions should reduce the computational cost.

5.6 Distribution
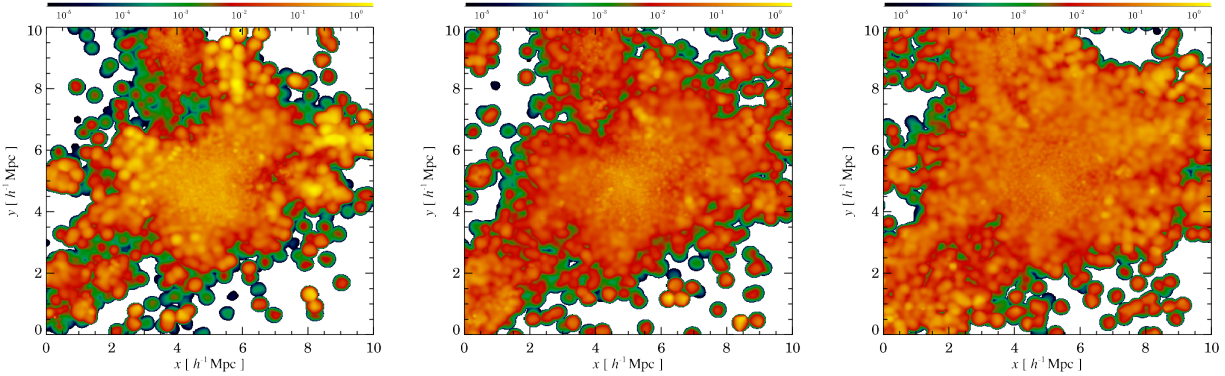
Figure 5.5: *Maps of metallicity for the enrichment model of (Tornatore et al., 2007) with three different wind models in a box with the indicated size. Left with no winds, the reference model in the middle and with strong winds on the right. Color coded appears the Fe abundance.*

There is no an explicit treatment of diffusion of metal mass and the contribution of each star particle is smoothed in the surrounding gas particles without to alter the total metal mass. The enrichment through SNe is hereby bulkier than the one from AGB-winds because of the time scale. AGB-winds represent a constant flux, while SNe distant events.

The used model for stellar winds gives the MZR its shape. In Daveé et al. (2006) is made a comparison between different wind models showing that the best match is achieved with a momentum-driven-wind model, which outflow velocity depends on the escape velocity of the

galaxies. A model with constant outflow velocity produced a flat MZR, understandable due to the prepolution of the IGM by smaller galaxies that cannot retain metals with strong winds.

Figure 5.5 illustrates the effect of the stellar winds in the distribution of metals. While the absence of winds produces an extreme concentration in the center and clumpy in the subhaloe of the represented cluster, the winds smooth and spread the metals and the effect increases with the speed of the winds.

6 Chemical Enrichment of Galaxies in MAGNETICUM

6.1 MAGNETICUM

MAGNETICUM is a set of hydrodynamical simulations designed to follow the formation and evolution of cosmological structures. Very large scale and computational expensive simulations as well as simulations of smaller volumes and higher spatial- and mass-resolution are performed to follow evolutionary processes at different scale- and resolution-levels. The last simulations are being performed on SuperMuc in Garching, by Munich, one of the most powerful supercomputer in Europe.

The used cosmology parameters can be found in Table 6.1.

H_0	Ω_0	Λ_0	σ_8	n
70.4	0.272	0.728	0.809	0.963

Table 6.1: *Cosmological parameters used in MAGNETICUM. From left to right, Hubble constant, matter density, cosmological constant, normalization of power spectrum and index of the primordial power spectrum (http://www.magneticum.org).*

The properties of the used resolutions in this work can be found in Table 6.2 and the rest of the properties of the used simulations in Table 6.3

	m_{dm}	m_{gas}	eps_{dm}	eps_{gas}	eps_{stars}
High Resolution (HR)	6.9e8	1.4e8	3.75	3.75	2
Ultra High Resolution (UHR)	3.6e7	7.3e6	1.4	1.4	0.7

Table 6.2: *Features of the used resolutions in this work. The first two columns tell the initial mass of dark matter- and gas-particles in units of $[M_\odot/h]$, respectively. The initial mass of star particles depends on the actual mass of the gas particles where they born from. The rest of the columns tell the corresponding gravitational softening for each particle type in units of $[kpc/h]$. Information about the rest of resolution levels offered by the MAGNETICUM simulations can be found in http://www.magneticum.org.*

The simulations use the code Gadget and include several physical processes to allow a reliable comparison with observational data. The following list show the used physics. This and further details about the MAGNETICUM set of simulations can be found in http://www.magneticum.org.

	Box3	Box4
[Mpc/h]	128	48
High Resolution (HR)	$2 \cdot 576^3$	$2 \cdot 216^3$
Ultra High Resolution (UHR)	*$2 \cdot 1536^3$*	$2 \cdot 576^3$

Table 6.3: *Features of the used simulations in this work. The first line tell the dimension of the box and the further lines the amount of particles used in each box to have the corresponding resolution level. The highlighted simulation for Box3 and HR is planned for the future. Further details about the complete set of simulations and their properties can be found in http://www. magneticum.org.*

- Cooling, star formation, winds (Springel & Hernquist 2003)

- Metals, stellar population and chemical enrichment SN-Ia, SN-II, AGB (Tornatore et al. 2003/2006)

- New cooling tables (Wiersma et al. 2009)

- Black holes and AGN feedback (Springel & Di Matteo 2006, Fabjan et al. 2010)
  Various improvements (Hirschmann et al. 2014)

- Thermal Conduction (1/20th Spitzer) (Dolag et al. 2004)

- Low viscosity scheme to track turbulence (Dolag et al. 2005)
  Various improvements (Beck et al. 2015)

- Higher order SPH Kernels (Dehnen & Aly 2012)

- Magnetic Fields (passive) (Dolag & Stasyszyn 2009)

The postprocessing algorithm *subfind* is used to localize haloe and subhaloe from the snapshots created by Gadget. The determined position of subhaloe are used as center of the galaxies and all gas- or star-particles inside some convenient radius are then analyzed to estimate the desired masses and metallicities of the galaxies.

Other useful galactic parameters like the virial radius R_{vir} and the star formation rate (SFR) are estimated by the postprocessing algorithm for each galaxy.

10% of R_{vir} is considered enough to analize each selected galaxy, since as explained in more detail in Section 3, the most of the stellar mass is inside this region. Some tests were done to proof how well other radius selections would reproduce the observations, like the selection of all particles only inside the effective radius R_{eff} or all particles starting from a confident radius dependent on the space resolution, i.e. the softening length for the corresponding resolution used. None of these selections showed to be a better choice to match the observational data.

6.2 Star Formation Efficiency

The star formation rate (SFR) reveals how much star formation (SF) occurs in a period of time, usually measured in solar masses produced per year and not in events. The common method to estimate this rate is by counting of events related to the SF activity. In molecular clouds is usual to count the young stellar objects (YSO). The later is calculated as following:

$$SFR(YSO) = N\_YSO \cdot \frac{<M>}{\tau} \qquad (6.1)$$

$<M>$ is hereby the mean mass of the observed YSOs in the galaxy and τ the lifetime of a YSO, namely $\sim$ 2 Myr (Ly et al., 2016).

The star formation efficiency (SFE) is a measure for the SFR per unit of gas mass. Evaluating if the SF activity in the simulations match the observational data is a key step to pretend to fit the mass-metallicity relation (MZR) with observations at different redshifts. In Figure 6.1 is shown the evolution of the SFE as observed until redshift z $\sim$ 2 in comparison with the obtained evolution in MAGNETICUM in the two analysed resolutions in this work.

There is a big scatter at each redshift because of the strong dependence of the SFR on the environment, but the global SFE clearly decay with the time. The comparison shows in principle an acceptable match inside the uncertainties visible in the observational data, but the higher values at higher redshifts for UHR resolution are showing an evident stronger star formation in early phases.

As pointed out in Tornatore et al. (2007), a higher resolution increases the cooling by a larger number of resolved haloe at high redshift, leaving a smaller amount of gas for subsequent SF. So, by higher resolution the SF is bigger first and lower then, but with nearly the same amount of stars formed. In the MAGNETICUM simulations, the feedback models still don't avoid efficient enough this characteristic extra SF produced by increasing the resolution.

Even if the difference between resolutions is small, this insight gives the key to understand the future discrepancies of the MZR with observational data. In fact, the effect of this early SF is reflexed in the higher metallicities obtained using UHR resolution, while in HR resolution they seem to fit closely. Since the number of formed stars is nearly stable, the overproduction of metals comes probably from stellar winds, which are simulated as still no exploding stars waiting their chance to build a binary system and become a SNIa. They have more time to enrich the environment.

6.3 Stellar Mass

The mass of the selected star particles can simply be taken and added up. Nevertheless, the estimation of the the stellar mass coming from the subfind algorithm represents a better approximation to the mass of the galaxy, since it takes into account that some stellar mass belongs to satellite galaxies. This acknowledgement cannot be easily done by just taking all particles inside some radius. In Figure 6.2 is shown a comparison of the stellar mass obtained by adding directly the mass of each involved star particle and the mass obtained from the subfind algorithm for a
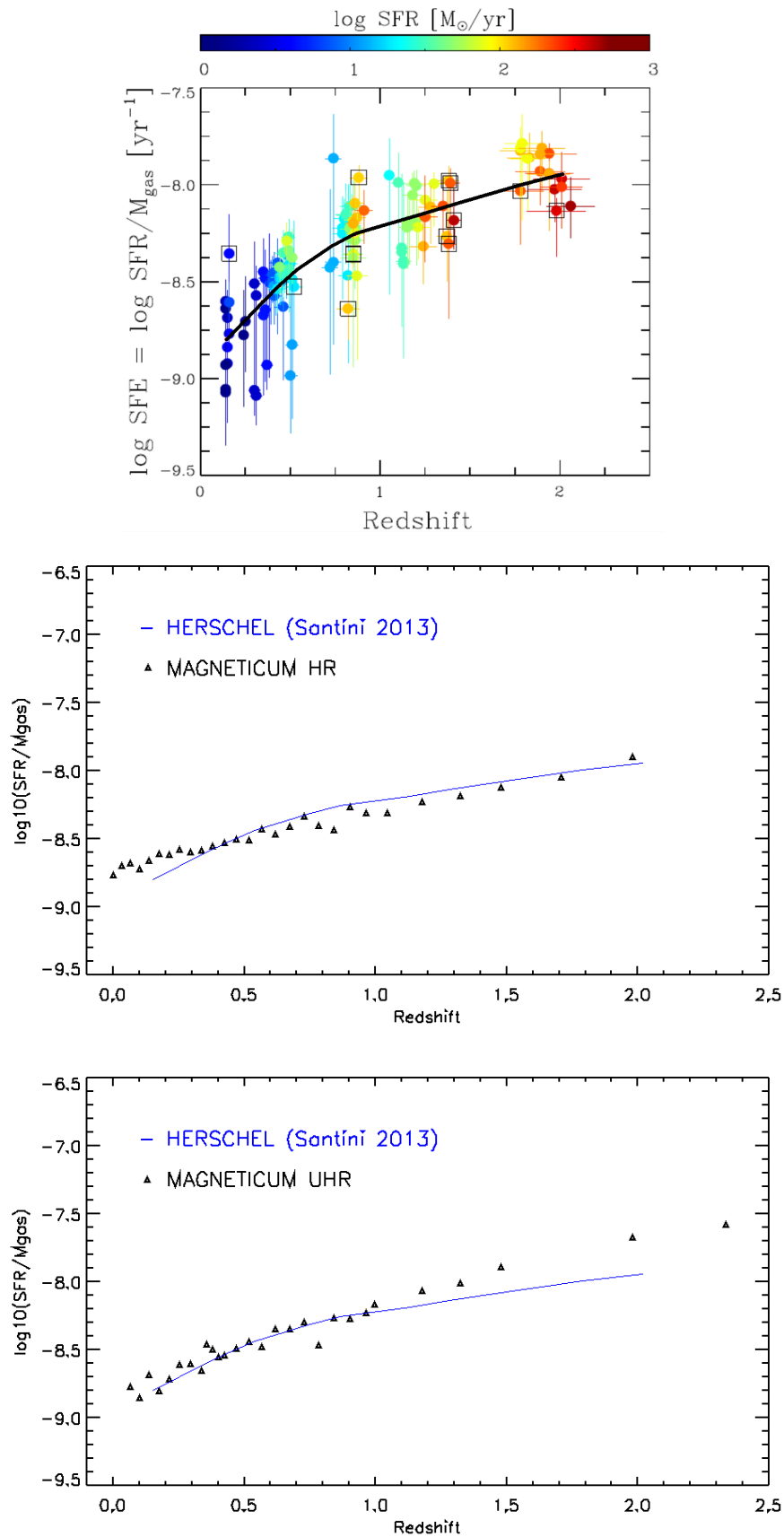
Figure 6.1: *Top: Evolution in time of the star formation efficiency taken from Santini et al. (2014). The black line was made carefully by hand in this work to provide a guide so close as possible to the median value at each redshift. Middle and Bottom: The blue line matches the black line in the upper panel. In the middle is the behavior for HR resolution and in the bottom for UHR resolution. There is slightly more star formation in early phases for UHR resolution.*

groups of galaxies of every kind in a wide mass range. The directly obtained values lie clearly above the postprocessing estimation, confirming the previous affirmation. Henceforth is used the stellar mass inferred in the subfind algorithm to plot the MZR against observational data.
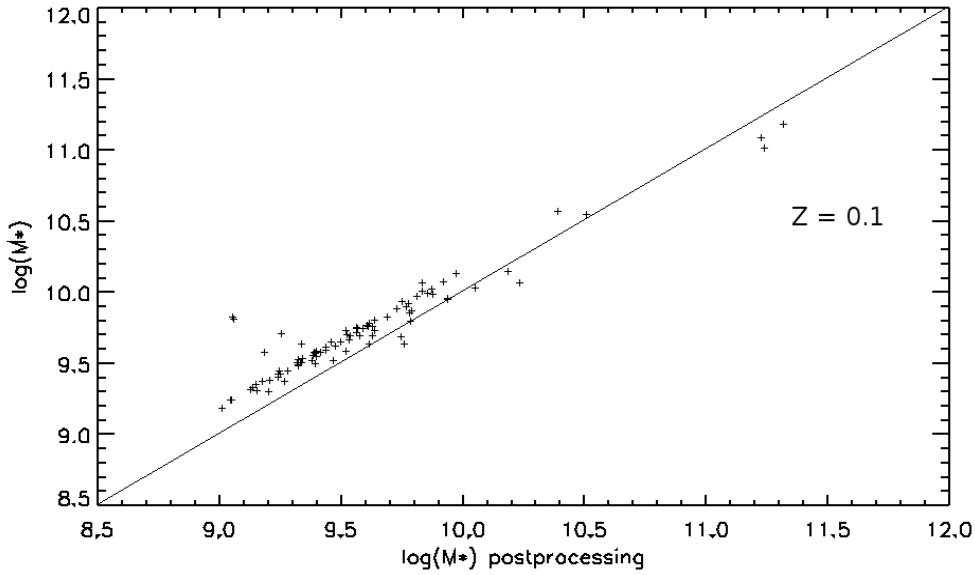
Figure 6.2: *Comparison of the galactic stellar masses calculated directly from all the star particles inside 10% of the virial radius R_{vir} and the estimation made by the postprocessing algorithm subfind. The later try to exclude potential satellite galaxies.*

6.4 Gas-Phase Metallicity

In the data coming from observations are made estimations of the number of atoms, as explained in Section 4.3, of the involved elements. The ratios used to describe the metallicities represent so the number ratio exposed in sections 2.1 and 2.2. From the simulations is exclusively to read the mass of each single element and the total mass, according to the model of Tornatore et al. (2007), so is still necessary, in order to make the right comparison, to make a conversion from mass ratio to number ratio.

To prevent giant numbers in atomic scales has been used since centuries the molar mass instead of the atomic mass. The molar mass is the mass of a *mole*, which represent a huge unified amount of particles of some kind, no matter which one, the number of atoms in our concern. This number was set by Avogadro to $N_A = 6.022 \cdot 10^{23}$ mol^{-1}.

This number was chosen to be the scale because the total mass of N_A atoms of the isotope C12 corresponds to exactly 12 g. The molar mass expressed in [g] of some element, then, corresponds almost to the number of nucleons in it, but is never exact not even in C, because it is meant to represent the mean value between the different isotopes of the element, weighted through their abundances. The molar mass for each element was estimated since then for each element and belongs to the basic information given in the periodic table of elements.

To find out how many atoms are present in some mass M_{tot} of an element, is used therefore the already known molar mass M_{mol} of this element, available in the periodic table of elements, to

get first the number of moles N_{mol} in this mass

$$M_{tot} = N_{mol} \cdot M_{mol} \tag{6.2}$$

To the mass ratio obtained from the simulations is therefore needed the following transformation using equation 6.2:

$$\frac{N_O}{N_H} = \frac{M_O}{M_H} \cdot \frac{M_{mol}(H)}{M_{mol}(O)} \tag{6.3}$$

The mass of each element divided by its molar mass throws the number of moles and the ratio of moles is also the ratio of atoms.

The total mass of O and H within a galaxy is calculated by adding the contribution of each single gas particle of interest. Afterwards, is calculated the number ratio according to Equation 6.3 and finally applied the definition of gas-phase metallicity given in Equation 2.1.

The gas-phase metallicity obtained through this method fit the observations for redshift 0 but doesn't show evolution, probably because of being the representation of a mean value among the all gas within the galaxy and not the recently enriched regions.

The same procedure is then applied to find the Fe abundance in the youngest stars and transform the values to gas-phase metallicity, as explained in Section 4.3.3, which represents the last stages of enrichment in the gas and makes possible the view of evolution.

The initial mass of star particles depends on the mass of the progenitor gas particle and both of them are moreover variable. As can be seen in Table 6.2, the starting mass of a gas particle in units of $M_\odot$ is $1.4 \cdot 10^8$ in HR resolution and $7.3 \cdot 10^6$ in UHR. Each gas particle can produce until 4 star particles, so, statistically is taken a fourth of the initial mass of gas particles as a reference for the mass of star particles, that is around $0.35 \cdot 10^8$ in HR and $1.9 \cdot 10^6$ in UHR, respectively, in units of $M_\odot$.

A BH in the center of the galaxy is produced with 1000 star particles, i.e. a stellar mass of around $0.35 \cdot 10^{11} \, M_\odot$ in HR resolution and $1.9 \cdot 10^9 \, M_\odot$ in UHR. That correspond in the logarithmic mass scale to ~ 10.5 and ~ 9.3, respectively.

In the aim of appreciate the limits of the mass resolution and their effects in the mass-metallicity relation (MZR), in Figure 6.3 are shown the metallicities in a wider mass range to show the behavior of the data beyond the tentative limit of mass resolution. The best bin choice to get a picture that is dense enough to note clearly the distribution of the data along the used mass range, was the separation in bins of 0.1 dex with maximal 100 galaxies per bin.

The comparison is done with observations at redshift $z \sim 2$, where is still enough massive spiral galaxies to cover generous the range of the HR resolution. The little amount of massive spiral galaxies at redshift zero responds probably to the big merger events that already have taken place.

In HR resolution is achieved a very good agreement, while in UHR resolution the behavior match the observations but with slightly higher values, evidencing the sensitivity to the used resolution shown in Section 6.2. The higher star formation (SF) that takes place in UHR resolution is
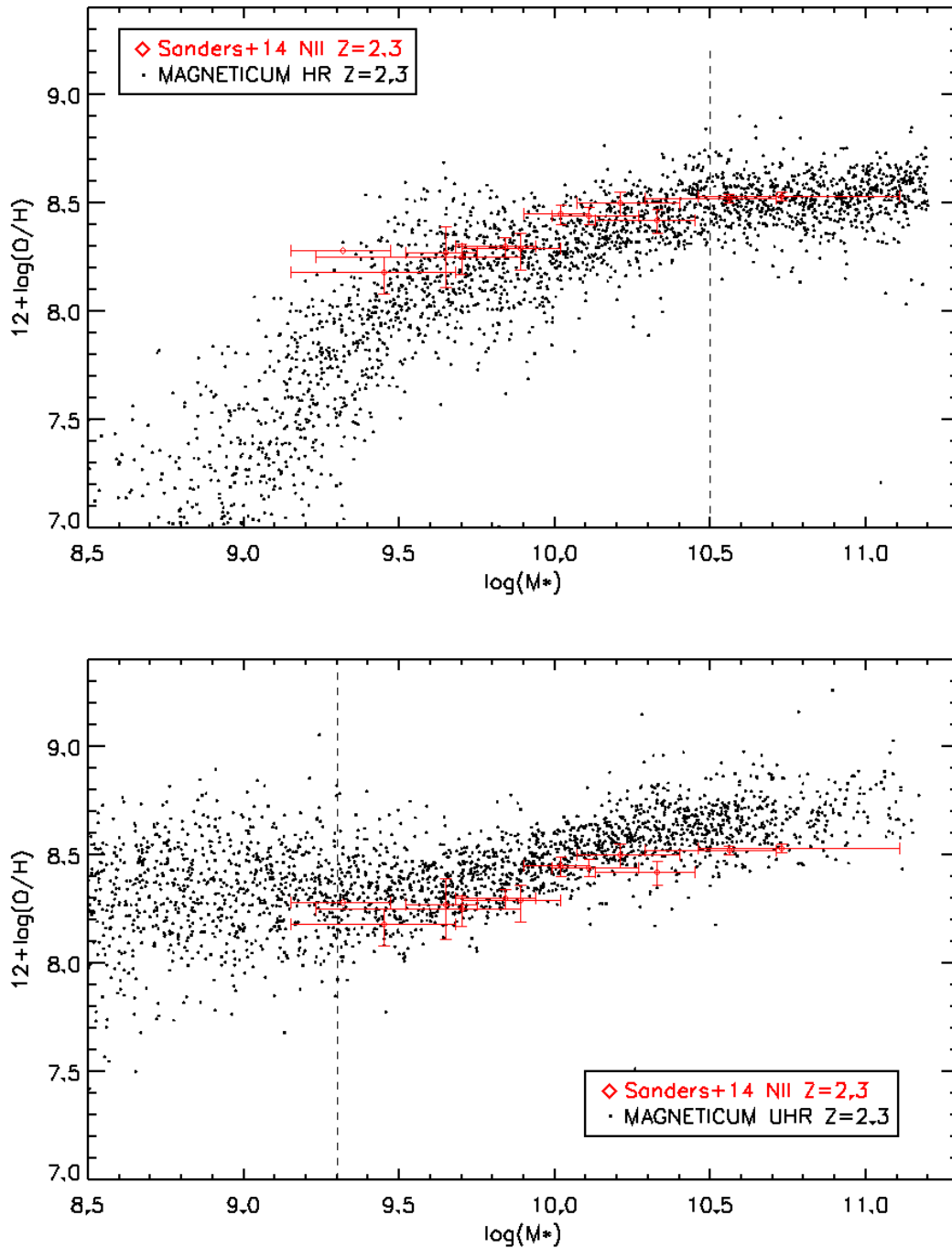
Figure 6.3: *Gas-phase metallicity in MAGNETICUM in comparison with the observational data from Sanders et al. (2015) at redshift z ~ 2, showing with a vertical dashed line the limit of the mass resolution, for HR resolution in the top panel and for UHR resolution in the bottom panel. Each black point represents a galaxy from the simulation.*

evidenced also in the higher values obtained in the MZR. If no further specification is given, is used the simulation in Box3 with HR resolution level.

The curve falls below the limit indicated with the dashed line. The fall is just a bit more accelerated than the one of the observational data, but they don't keep any relation anyway. The reason of the metallicity decay with the lack of resolution lies by the also lack of physics necessary for SF activity. In galaxies below the resolution limit are probably just a handful of gravitational bounded particles, recognized for the subfind algorithm as a subhalo. The density of particles here is again not enough neither to trigger enough SF nor to boost a characteristic interaction in a SF region.

6.4.1 Evolution

The key to understand the observation of evolution lies in the principles of the young stellar metallicity method, explained in Section 4.3.3. In this method are selected the newest stars of a galaxy to infer the gas-phase metallicity in a very last stage of the galaxy, namely when these stars were born. This method is not just free of the possible systematic errors by observing the galactic nebulae, but show precisely the abundances in the star forming regions. Any other discrimination of the gas particles in simulations doesn't take in account if this particle was enriched lately or in an early stage. The key to select the galactic regions suitable for compare with observational data doesn't lie in the features of the ISM gas, but in the recent stellar activity.

The stellar metallicity of all star particles younger than 100 Myr was averaged and then transformed to gas-phase metallicity, following the transformation of Bresolin et al. (2016) presented in Section 2.2. The results show in fact the newest metallicity values of each galaxy and a clear evolution with redshift.

Figure 6.4 shows the evolution from redshift $z \sim 2.3$ to redshift $z \sim 0$ with bins of 0.1 dex and 1000 galaxies per bin, to appreciate at the best the distribution of the data. The median of the values is also shown, with an amazing concordance with the observational data.

6.5 Stellar Metallicity

The mass of Fe and H and the respective number ratio, needed to represent the stellar metallicity as shown in Section 2.2, is obtained in the same way as the O/H ratio for the case of the gas-phase metallicity. In this case is not added up all the content in the galaxy before to apply Equation 2.2, but calculated the number ratio for each star particle and then the mean value, since the stellar metallicity represent the mean metallicity of the stars within the galaxy.

Remarkable is that each star particle is not a single star, but a star population, limited by the space- and mass-resolution of the simulations. Nevertheless, all stars in the population are supposed to have the same age and initial metallicity. So is made the approximation that the metallicity of the star particle represents a mean value between the stars that belong to the population.

In Figure 6.5 is shown the mass-metallicity relation (MZR), like in the case of gas-phase metallicity,
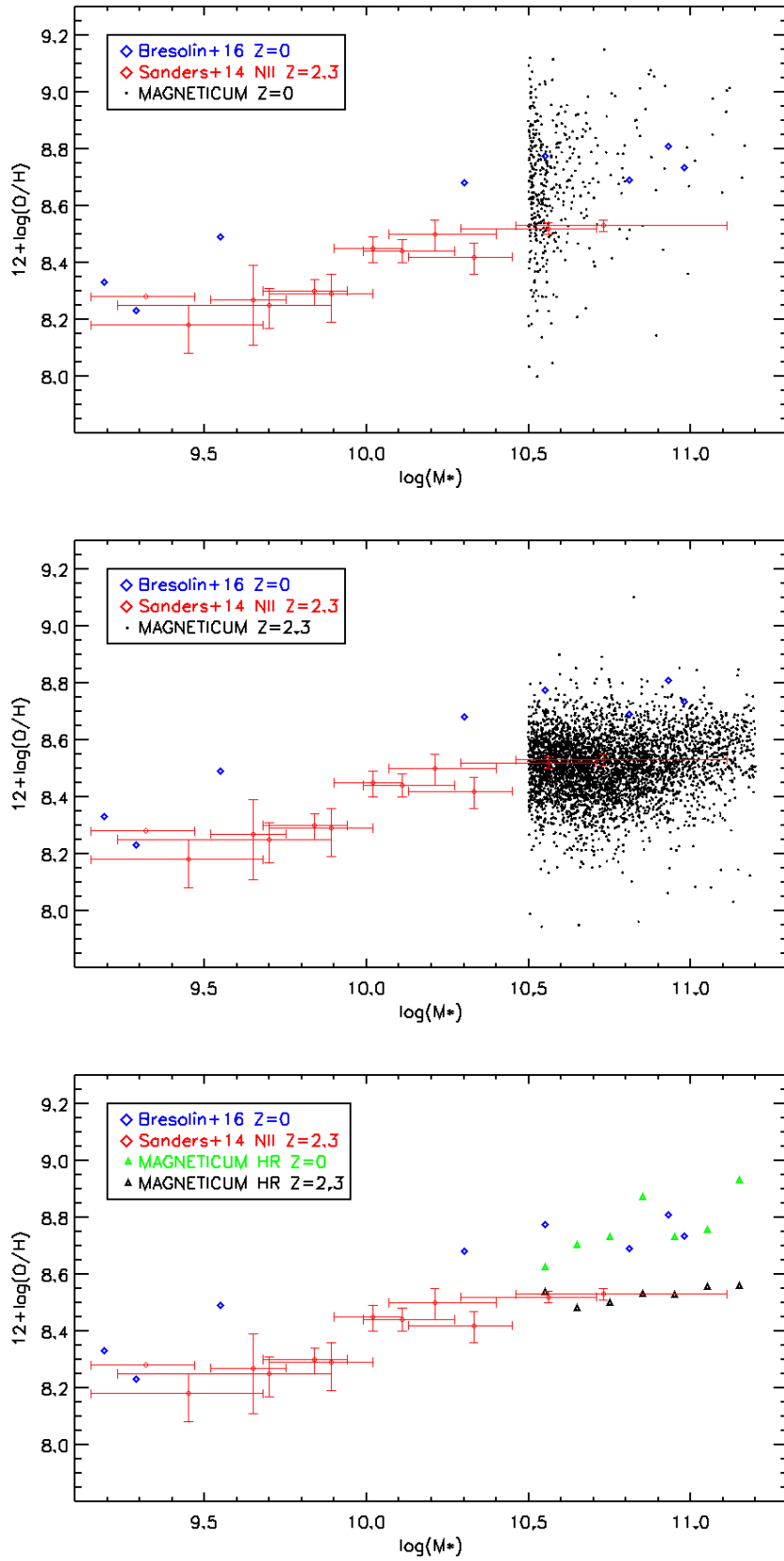
Figure 6.4: *Evolution of the gas-phase metallicity in MAGNETICUM in comparison with the observational data presented in Sanders et al. (2015) and Bresolin et al. (2016). In the top panel is the distribution of galaxies at redshift z ∼ 0. Each black point represents a simulated galaxy. In the middle panel the same plot with the data obtained at redshift z ∼ 2.3. In the bottom panel is drawn with triangles the position of the median values for each mass bin in each case.*

for HR and UHR resolution, showing the limits of the mass resolution. As can be seen in the picture, there are more problems reproducing the slope of the stellar MZR. In general appears too flat in comparison to the observations. The generally flat and thin scatter of the stellar metallicity makes moreover meaningless a separated analysis between spirals and ellipticals galaxies, which can be found in observational data.

Like in the case of gas-phase metallicity, the fall of the metallicities in HR resolution is more dramatic. In UHR resolution the values are just slightly higher. The difference is smaller than for the gas-phase metallicity, probably because not all the metals overpolluting the IGM are translated in the metallicity of the new built stars.

6.6 Gas-Phase Gradients

To make a proper comparison of the gradients with observational data is necessary to calculate first the effective radius R_{eff} of each galaxy, the scale radius selected by the most observations of gradients. In this concern, all selected particles within a galaxy were ordered with increasing radius. Then, the masses were added until to reach the half of the total stellar mass. The corresponding radius at this point represents R_{eff}. As R_{eff} is therefore taken the radius at which the half of the stellar mass is contained, within the 10% of the virial radius R_{vir}, previous selected.

For making the gradients, the metallicity at each radial position is averaged between many galaxies. It was shown to give the best picture a configuration of 100 radial bins per R_{eff}.

The comparison is made with the observational data from Sánchez-Menguiano et al. (2016), showed in Figure 3.1, where the metallicities are estimated with the O3N2 method. The conversions offered in Kewley and Ellison (2008) are applicable only in a lower mass range than the exposed in this gradient. For high masses, nevertheless, The NII calibration as well as the O3N2 calibration are close enough to the more reliable young stellar metallicity method, as explained in more detail in Bresolin et al. (2016). The comparison can be seen in Figure 4.4.

This analysis is made in Box4 and UHR resolution to exploit the space resolution needed to examine the radial range and learn so much as possible about the behavior of the gradients out of the simulations, and knowing the concordance in the behavior of the mass-metallicity relation (MZR) and just slight higher values for UHR resolution.

The radial profiles are first calculated for the whole radial range to appreciate the limitations of the resolution, this time of the space resolution. As can be seen in Table 6.2, the softening length for gas particles in UHR resolution is 1.4 kpc/h. Considering this, the 2 innermost kpc are taken as not trustable for the tests.

Figure 6.6 shows two versions to be compared. The first version removes the 2 innermost kpc that are not to trust for UHR resolution and the second version take all particles and indicates the mean position of the 2 kpc limit, since the radial profile is normalized to the R_{eff}. The space resolution limitation doesn't show a big impact like the one of mass resolution.

Figure 6.7 shows the radial profile leaving the 2 innermost kpc away, corresponding to the space resolution constraint, but also making the same mass bins separation as in the Graphic from Sánchez-Menguiano et al. (2016). The lower metallicities in the mass region that includes the
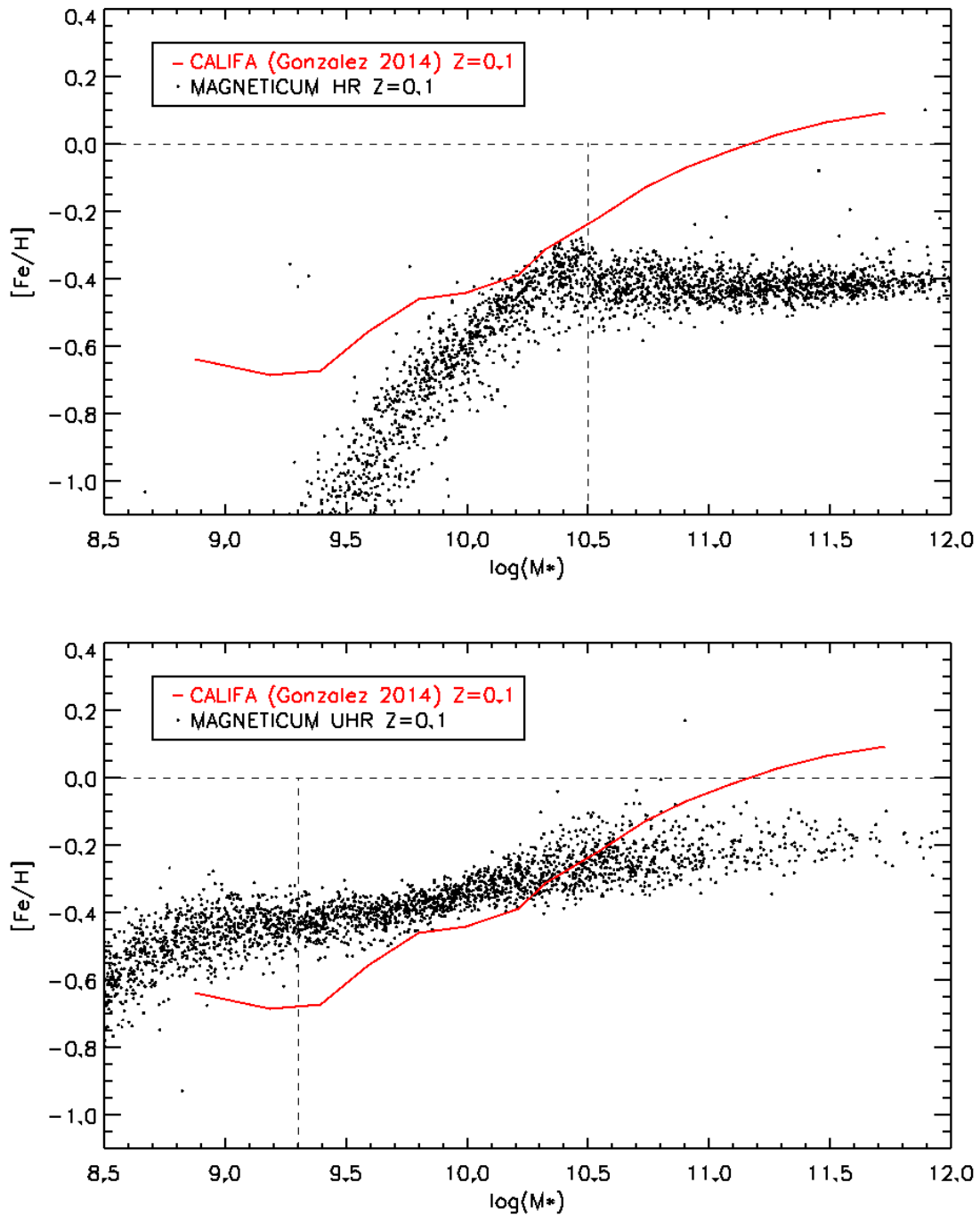
Figure 6.5: *Stellar metallicity in MAGNETICUM in comparison with the observational data of all kind of galaxies taken from González Delgado et al. (2014) at redshift z = 0, showing with a vertical dashed line the limit of the mass resolution. Each black point represents a simulated galaxy. In the top panel for HR resolution and in the bottom panel for UHR resolution.*
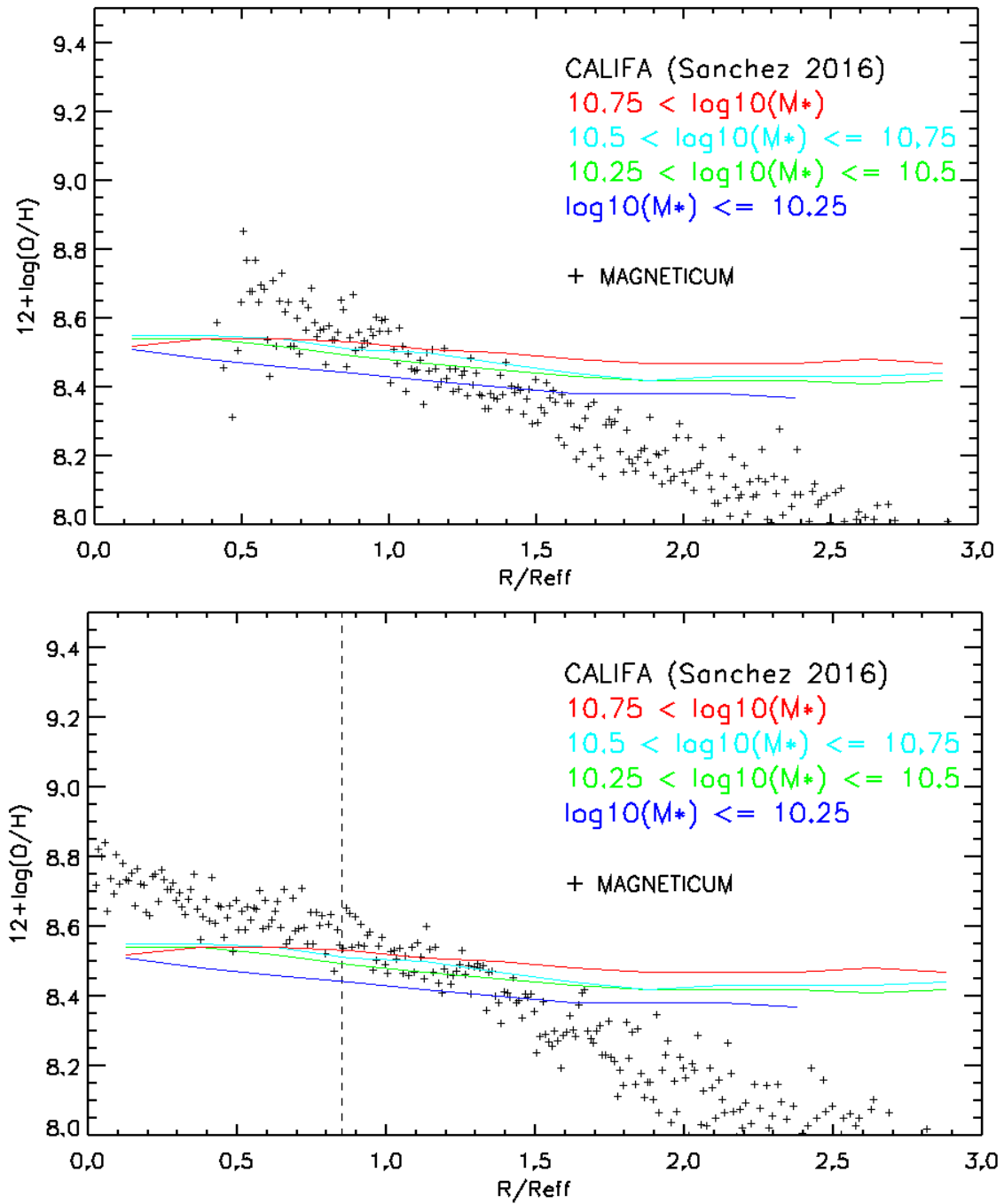
Figure 6.6: *Gas-phase metallicity gradient in MAGNETICUM compared with the observational data presented in Sánchez-Menguiano et al. (2016). From the simulations is obtained mean values among 100 galaxies in 100 radial bins per effective radius R_{eff}. In the top panel is suppressed the 2 innermost kpc correspondent to the space resolution limit in UHR resolution, while in the bottom panel are included, but indicating the mean position of the space resolution limit after normalization to the R_{eff}.*

region of the simulation with lack of mass resolution are evident. For the rest of mass bins the behavior is as expected from the MZR, with the most massive galaxies showing higher values. Each mass bin keep the original slope, discarding any possibility of being the mass mixture the reason for the steeper slope.
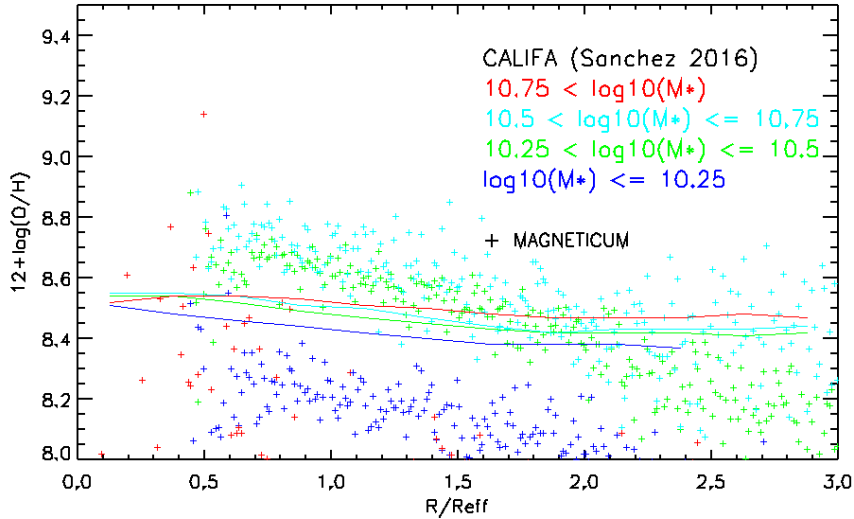

Figure 6.7: *Gas-phase Metallicity Gradient obtained in MAGNETICUM, compared with the observational data from Sánchez-Menguiano et al. (2016). The colors indicated in the graphic correspond to the mass region for the fits from the observations, as well as for the simulation radial bins.*

As expected from the behavior of the MZR and also observed, the more massive the galaxies are, the higher metallicities they show. A clear averaged slope is also shown, when they are normalised through the R_{eff}, confirming the good choice predicted theoretically and used to normalize observational data. The gradients are in general steeper than the observed ones. More metals are placed near the core of the galaxies and less in the outskirts, probably because of the effect of strong galactic winds at higher radii. The most massive bin sinks strongly in the inner region. Possible reasons for these behaviors are discussed in Section 7.

Further tests were done, in order to find out a possible needed constraint not taken in account for a reasonable comparison. Observations of gas-phase metallicities are done in HII regions characterized for reaching a temperature of around 10^4 K and a minimal abundance of H of about 70%. This conditions are added to the selection constraints of the ISM gas in the simulations and compared with the observational data shown in Figure 3.1. These tests are done using the version that leaves out the 2 innermost kpc related to the space resolution in UHR. Figure 6.8 shows the results.

Warmer gas was expected to contain more metals, since the warm regions in the IGM are thought to gain their mass and energy mostly from close recent stellar activity, being more enriched than the rest of the environment. The results confirm that clearly too warm gas is newly enriched and throw a chaotic behavior with high enriched values, while the cold gas version is more alike to the version with no temperature constraint. The condition of high H abundance sinks the inner region of the gradient, probably because the longer SF activity that consumed the ISM gas near the center of the galaxy. The mixed constraints don't show a special feature.
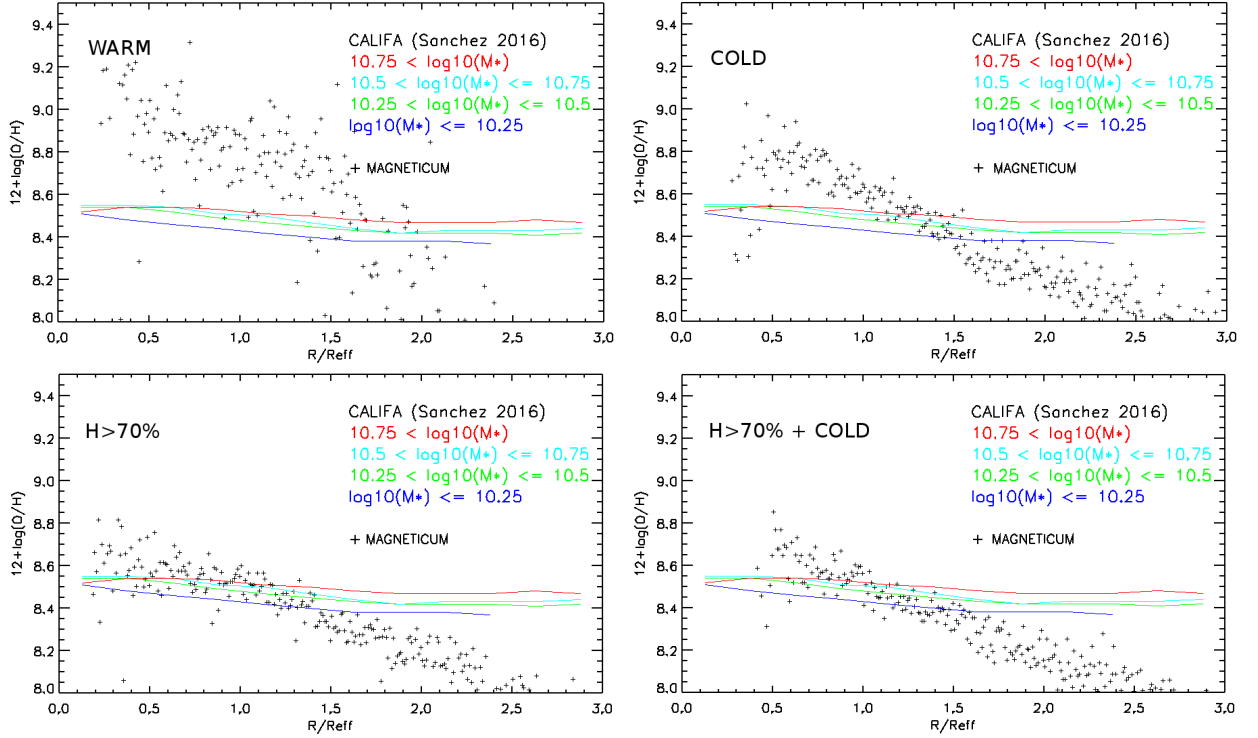
Figure 6.8: *Top left: Gas-phase metallicity gradient in MAGNETICUM by taking just gas above 10^4 K in comparison with the observational data from Sánchez-Menguiano et al. (2016). Around this temperature should be reached in HII ionised regions, where observations of gas-phase metallicities take place. Top right: Same comparison, but with gas below this temperature. Bottom left: behavior of the gradient by just taking the gas with a composition of minimal 70% of H, which is expected in HII regions. Bottom down: A mixture constrain between cold enough and and H rich ISM gas.*

6.7 Stellar Gradients

In comparison with the gas-phase metallicity, the stellar metallicity obtained from the simulations reproduce very well the observed gradients. We use the simulations with HR resolution in the following analysis, to the detriment of the space resolution, using this to make a comparison as close as possible with the observational data.

The softening length for star particles in HR resolution reaches 2 kpc/h, as shown in Table 6.2. The same test is made for stellar gradients taking this time also 2 kpc as tentative limit of space resolution.

Figure 6.9 shows the results. The discrepancies between the observations and the simulated profiles start by the vertical dashed line that indicates the limit of the space resolution. This shows how in this case, where the gradient is well reproduced, the space resolution does play a role. The version leaving out the stars in the 2 innermost kpc is still not free of values under the expected mean values, but shows less population in this region. Probably a bigger constraint is needed. Some authors point out a region of confidence starting by 3 times the softening length.

Figure 6.10 shows the dispersion obtained in the stellar metallicity gradients with 1, 10 and 100 galaxies. The dispersion is nearly the same for every galaxy and reaches between 0.3 and 0.6 dex. The higher the number of galaxies, the regular the mean values per radial bin becomes, as well
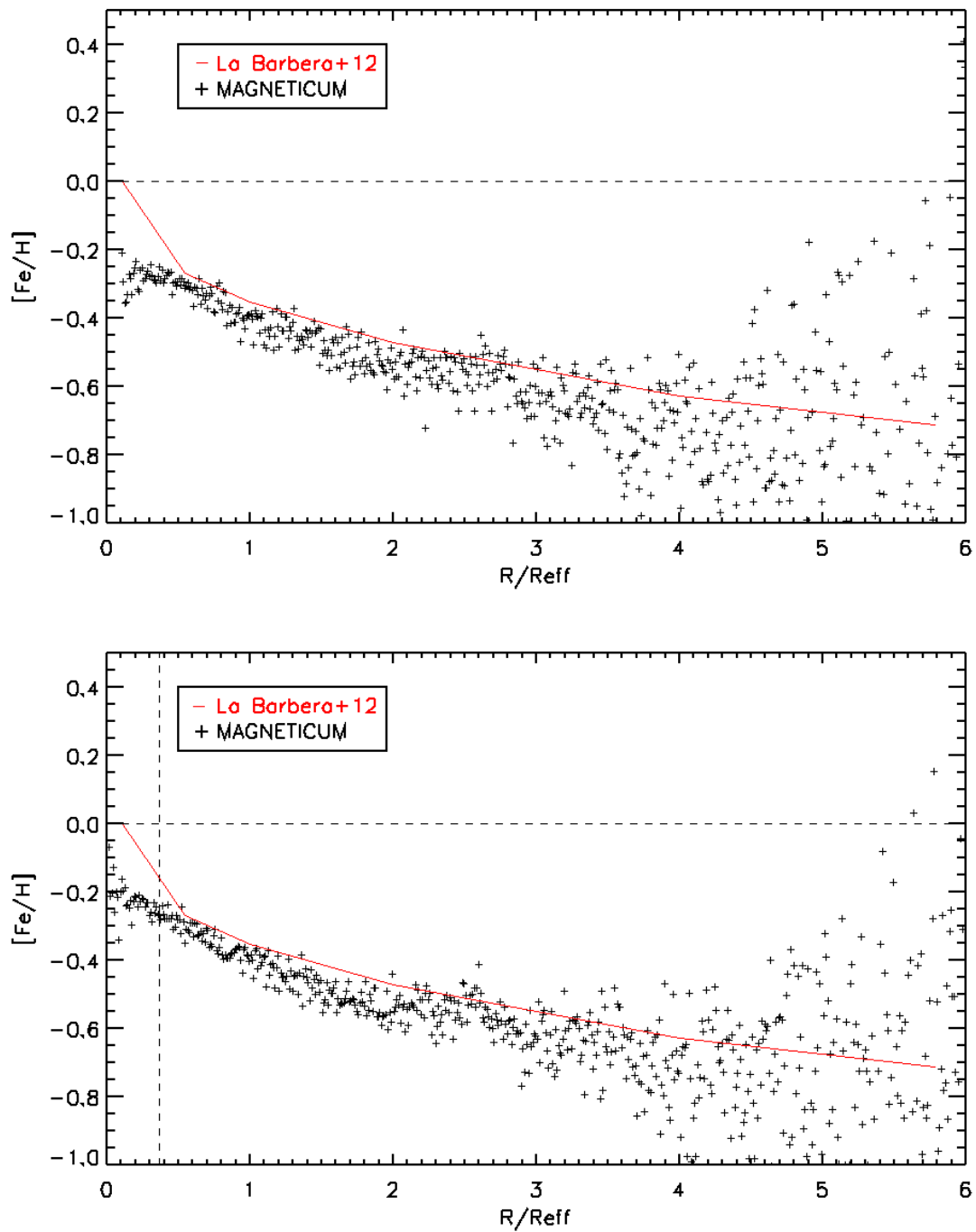
Figure 6.9: *Stellar metallicity gradient in MAGNETICUM compared with the observational data presented in Sánchez-Menguiano et al. (2016). From the simulations is obtained mean values among 100 galaxies in 100 radial bins per effective radius R_{eff}. In the top panel is suppressed the 2 innermost kpc correspondent to the space resolution limit, while on the bottom panel are included, but indicating the mean position of the space resolution limit after normalization to the R_{eff}.*

as the curve of the median values becomes, but without to change the total dispersion.
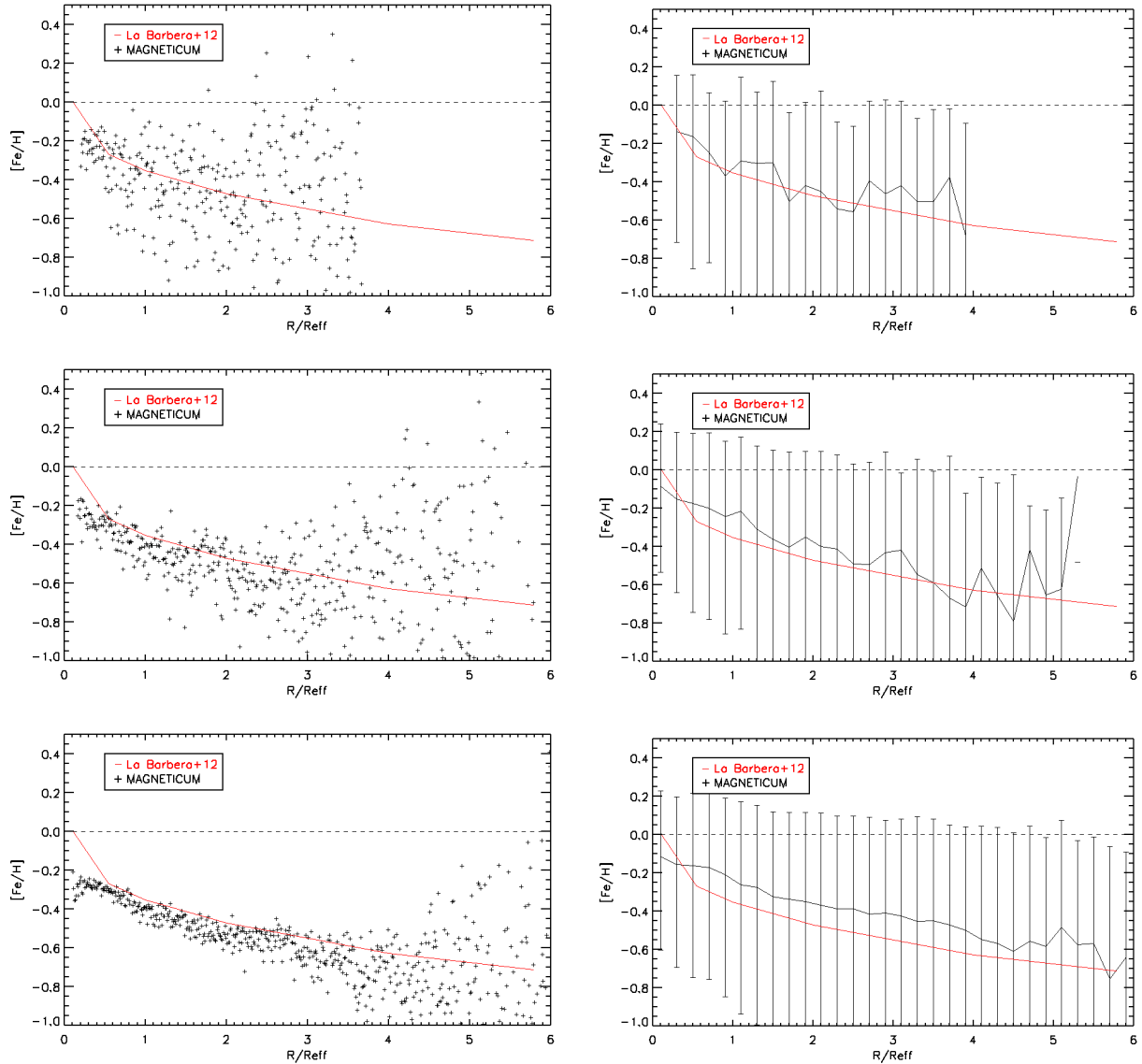
Figure 6.10: *Dispersion seen in the stellar metallicity gradients in MAGNETICUM. In the left panels are shown the gradients with the usual bining of 100 bins per effective radius R_{eff}, while in the right panels are shown the curve of the median values, by using only 5 bins per R_{eff}, with error bars representing the dispersion with 15% and 85% percentiles. Top: examples with 1 galaxy. Middle: 10 galaxies. Bottom: 100 galaxies.*

Interesting to notice is how, while the mean values lie slightly below the observed ones, the median values lie above. The latter means that although the most stars have metallicities a bit over the observed values, the metal poor outsiders are more extreme, and the responsible for the slightly mean lower enrichment seen in the stellar mass-metallicity relation (MZR).

In Figure 6.11 is shown the stellar metallicity gradients of four elliptical galaxies. The gradient used in this work for comparison, from La Barbera et al. (2012), represent a good mean behavior for these galaxies. From these samples, moreover, can be taken typical dispersion values at radius 1, 2 and 3 R_{eff} by comparing the extreme values, and they match the obtained dispersion in MAGNETICUM between 0.3 and 0.6 dex, showed in Figure 6.10.
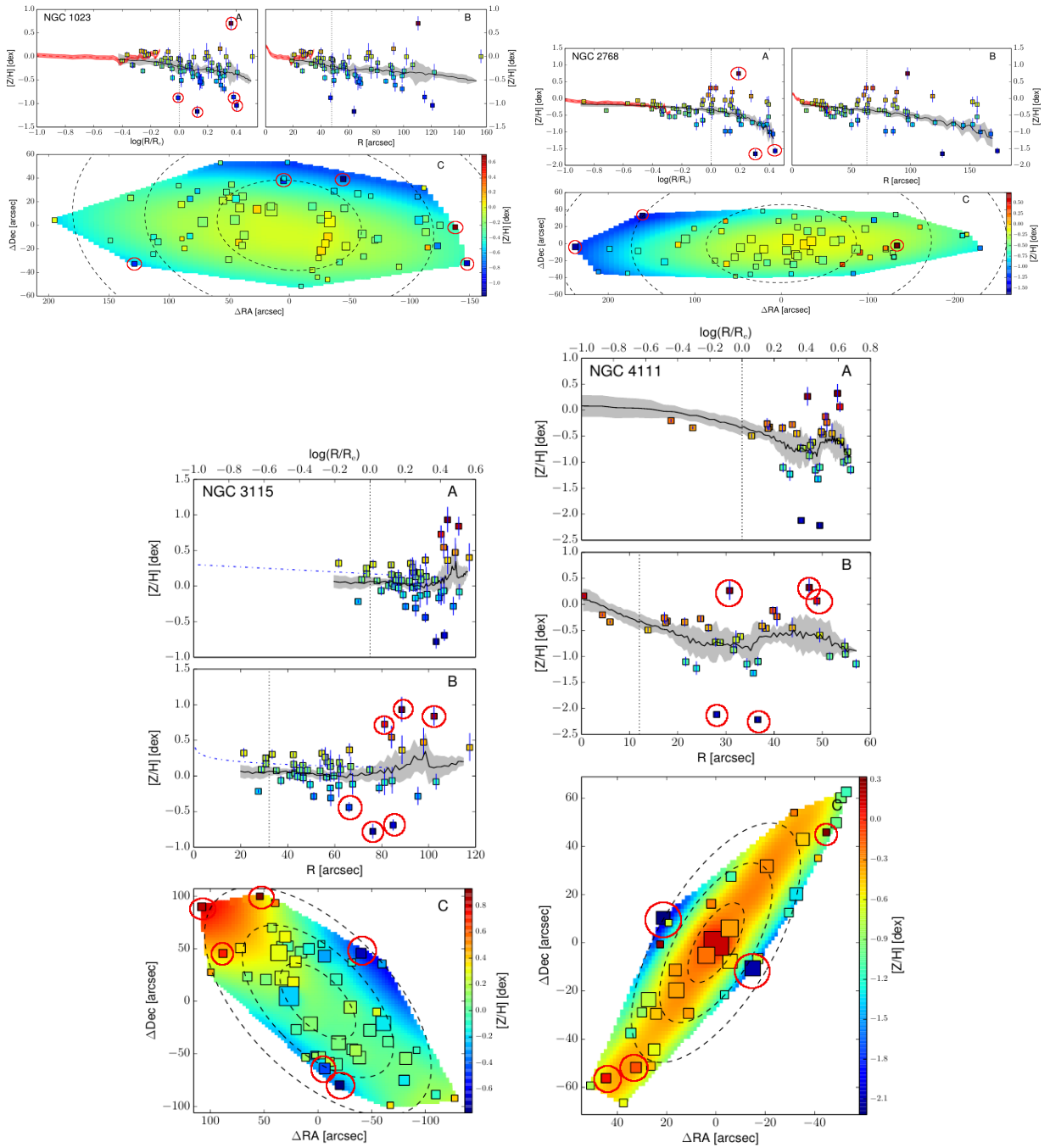
Figure 6.11: *Stellar metallicity gradients from the four elliptical galaxies indicated in the respective panel, taken from Pastorello et al. (2014). In the top sub panels are represented the radial profiles inferred from the study, normalized to the effective Radius R_{eff} and absolute. In the lower subpanels are indicated with square symbols the position of the measurements, color coded according to the metallicity and with a size inversely proportional to the associated uncertainty. The pixel fill of the region is the result of the interpolation of the measurements. The galaxies are not face-on, reason why the gradient in the minor axis appears steeper. The dashed lines represent hereby the galaxy isophotes with circularized radius R = 1, 2 and 3 R_{eff}. The red circles added in this work, indicate the extreme values that appear in the outskirts and don't follow the trend, representing probably members of satellite galaxies or outsiders.*

6.8 behavior of Further Elements in Stars

It was also a goal to look at the behavior of further individual elements produced with this chemical enrichment model. In Ryde et al. (2016) are presented measurements with the very large telescope (VLT) of Mg/H and Si/H stellar metallicity ratio against the common Fe/H ratio at 100, 200 and 300 kpc galactocentric distance in the Milky Way (MW). The MW has ~ 700 pc until its effective radius R_{eff}, so in this work is made a comparison with simulated MW-like galaxies until 3/7 R_{eff}.

In Ramírez et al. (2013) is made a similar analysis with the O/Fe ratio. In that work is made the separation between thin disc and thick disc. The thin disc of the galaxy is where the star formation (SF) is higher. The most stars and also the youngest, are placed in the thin disc. The thick disc go farther away and has older stars. There is still no way to do such a difference in a simulation specialized in cosmological resolution levels, but the positions of both curves still work as a guide for the general behavior.

In Figure 6.12 are shown the results. The observational data represent values of individual stars, while the data from the simulation represents the mean values between all stars in MW-like galaxies placed until 3/7 of their R_{eff}, separated in Fe/H bins.

The results in all three cases are similar. There is a clear trend in all similar plots of increasing the individual elements abundance for under solar values of Fe/H. That means that the decrease of Fe abundance, mostly by increasing the galactocentric distance, is steeper in the case of Fe than in the case of typical elements produced by SNII. This distribution, explained in more detail in Section 3.2, is even more emphatic at bigger scales. In the simulations, however, this distribution is not well reproduced. This reveals how the abundance profiles of other typical SNII products, like the ones of O presented in Section 6.6, are also steeper than the observed ones.
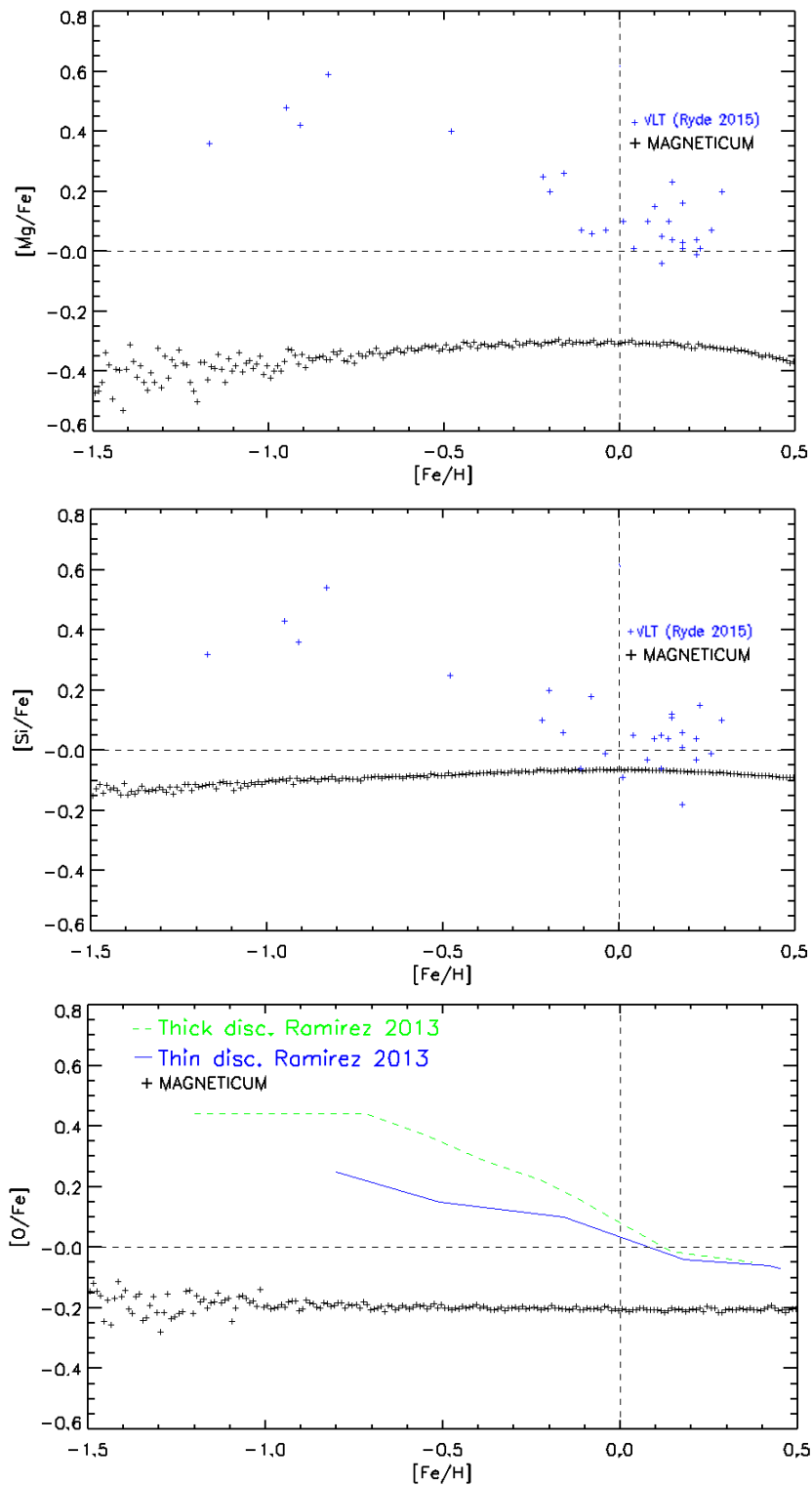
Figure 6.12: *Top and Middle: The indicated relations presented in Ryde et al. (2016) for Mg and Si abundances in stars, respectively, in comparison with the MAGNETICUM flat behavior. Bottom: Similar analysis with the observational data presented in Ramírez et al. (2013) for O.*

7 Discussion

In Chapter 2 is described the evolution of the mass-metallicity relation (MZR) as we can learn from observations. From the evolution of the enrichment alone, we gain a global picture of galaxy evolution, also supported for several observables. The fact that the slope of the MZR flatten with the time, points to an early galaxy growth through merging of small systems with low star formation (SF). A stronger SF and metallicity evolution occurs only later when the ensembles are big enough, enriching also the environment where other small galaxies live, accelerating their enrichment with more metals inflow. In the high mass end instead, there is an evident slower increment of the enrichment, since galaxies end up reaching the quenching stage, where they run out of gas to keep forming stars.

As shown in Figure 4.1, with observations out to redshift $z = 2$, there is a clear tendency of the star formation efficiency (SFE) to sink with the time, always faster. How it happens cannot be fully answered, but probably all galaxies end up to enter a quenching process. The scatter in these observations is also very big, suggesting that at fixed redshift, the star formation rate (SFR) of a galaxy is strong dependent on the environment, e.g. if it is getting closer to the center of some cluster or victim of a big merger.

Since the awareness of the MZR it has been tried to correlate these parameters with the SFR. In general is not a good idea trying to find a MZ-SFR relation. The actual observed metallicity depends on the entire history of gas in- and out-flow of a galaxy and the related SFR, while the actual observed SFR is only the actual one, and as shown in Santini et al. (2014), evolves with time and with a big scatter. As found in several works (Ly et al., 2016), a dependence in the MZR on the SFR for a fixed redshift is weak, surely because of this mentioned big dispersion in the SFR and unlucky selections of galaxies.

Only the current stellar mass is a truly good evidence of SF activity through the galactic history, including the accreted regions, and that makes the MZR the most meaningful correlation involving metallicity. The MZR can be seen as universal with slightly deviations dependent on the age of virialization of the galaxies and stronger but meaningless ones dependent on the SFR.

In this work was shown, how the discrimination of the gas by temperature or composition show no substantial change in the gas-phase MZR and gradients. The method proposed in Bresolin et al. (2016), and used in this work, showed that the most appropriate comparison with observational data is made using the time of enrichment as selection criterion. The HII observed regions are usually recently enriched regions and show the highest metallicity in the galaxy. There is no way to extract of the simulation, at which moment a gas particle was enriched, making the young stellar metallicity method the most appropriate to estimate gas-phase metallicities.

Thanks to this improvement in the analysis and the power of the MAGNETICUM simulations, this work shows the first simulated evolution in the MZR that reproduce the observations in the range $z = 0$-2.

Observationally, this young stellar metallicity method is the best method to find the gas-phase metallicity in nearby galaxies, where is possible to measure the metallicity out of the stars. For higher redshifts are the NII and O3N2 strong-line methods recommended, which fit at the best this method, at least by the high mass end.

A possible scenario to explain the flatness of the stellar metallicities can be put down to the role of the initial mass function (IMF) in the enrichment model of Tornatore et al. (2007). The use of the IMF to approximate the effects of stellar activity is widely spread because the impossibility to resolve single stars with the actual resolution power. An apparent good immediate approximation is achieved, but the procedure can have consequences in long term.

Through the IMF is decided how many massive stars are ready for a supernova (SN) explosion within a stellar population. The most massive stars end up first as SNII, while a SNIa takes longer to happen. When a SNII takes place, the amount of lost mass is reduced from the star particle, hence from the whole stellar population. In a next time step, the IMF is estimated for the whole population again with the new mass and the number of stars is reduced for each region and not only for the mass region where a group of stars was actually reduced, reducing the contribution of less massive stars and the products of SNIa. The bigger and the older the galaxies, and the more massive the populations after a long SF process are, the higher the lost of SNIa production, maintaining a nearly flat behavior instead of increase like in the observed MZR. O (SNII product) gradients instead, appear overreached in the center of the most massive galaxies.

In addition, according to observations, the behavior of the IMF in the local universe seems to vary by crossing the threshold of 1 $M_\odot$. As exposed in Tornatore et al. (2007), some arguments suggest that this typical scale value could be heavier in the past, making the form of the IMF time dependent and a source of discrepancies in the seen abundances and profiles.

The gas-phase metallicity gradient in the simulated galaxies fail in reproducing the typical flat regions seen in observations. Radial migration is a proposed theory to explain the flatness. If radial migration is responsible for this behavior in the profiles, then is a feature that is not well simulated and an interesting subject of test in future analysis.

The steeper O abundances, as well as the similar behavior of other SNII products in comparison to Fe, are probably caused because too strong winds at higher radii. Close to the center instead, looks overreached, and the total metallicity match the observational data. If the winds throw away the metals at higher radii more effective than one could wish, than was the process also more effective in early times, when there were smaller galaxies in average, overpolluting the IGM. This overpollution, also reported in other similar simulations, could be the reason of the overenrichment in the inner region, since the galaxies formed in an already overenriched environment. The result of this scenario is a global reasonable metallicity with steeper gas-phase metallicity gradients.

Fe in the other hand, is not expelled by AGB-winds and in general less distributed and affected by them, which is probably the reason why the stellar metallicity gradients are very well reproduced. Thanks to the MZR and the obtained gradients are found the possible improvements in the feedback models, learning about them and building an even more powerful tool to further studies.

There are still issues to solve with the galactic feedback models to achieve results, resolution independent in this single case, but in general much to test and constraints to do for the future, in order to reproduce all the observables that reveal galactic evolutionary processes.

Bird et al. (2016) show how the increment of the energy in SN models, using the Illustris simulation, helps to fit profiles of C obtained from absorption lines in quasars. The increment of energy in the winds can be achieved incrementing its speed, but that reduces at the same time the SFE. It is shown how transforming a part of the energy in heat, instead of acceleration, is achieved a better fit in the profiles without to disturb the SF activity. Nevertheless, this improvement just reproduce good the observations around low-mass haloe and not around big massive objects. It was proposed to change the AGN feedback model for further chemical enrichment without to warm the gas too much. We can learn from these cases how inaccurate the used feedback models still are, by reproducing universally a wide range of galaxies. The energy and mass produced by all the galactic feedback processes are intrinsic connected and the way they manifest, as well as the interplay between them, has to be still better understood.

References

Andrews, B. H. and Martini, P. (2013). The Mass-Metallicity Relation with the Direct Method on Stacked Spectra of SDSS Galaxies. *Astrophysical Journal*, 765:140.

Bird, S., Rubin, K. H. R., Suresh, J., and Hernquist, L. (2016). Simulating the carbon footprint of galactic haloes. *Monthly Notices of the RAS*, 462:307–322.

Borgani, S. et al. (2008). The Chemical Enrichment of the ICM from Hydrodynamical Simulations. *Space Science Reviews*, 134:379–403.

Bresolin, F. et al. (2016). Young stars and ionized nebulae in M83: comparing chemical abundances at high metallicity. *ArXiv e-prints*.

Bruzual, G. and Charlot, S. (2003). Stellar population synthesis at the resolution of 2003. *Monthly Notices of the RAS*, 344:1000–1028.

Chiosi, C., Merlin, E., and Piovan, L. (2012). The Origin of the Mass-Radius Relation of Early-Type Galaxies. *ArXiv e-prints*.

Daveé, R., Finlator, K., and Oppenheimer, B. D. (2006). The Mass-Metallicity Relation in Cosmological Hydrodynamic Simulations. *ArXiv Astrophysics e-prints*.

Denicoló, G., Terlevich, R., and Terlevich, E. (2002). New light on the search for low-metallicity galaxies - I. The N2 calibrator. *Monthly Notices of the RAS*, 330:69–74.

Erb, D. K. et al. (2006). The Mass-Metallicity Relation at z $\overset{\sim}{>}$ 2. *Astrophysical Journal*, 644:813–828.

Gallazzi, A. et al. (2005). The ages and metallicities of galaxies in the local universe. *Monthly Notices of the RAS*, 362:41–58.

González Delgado, R. M. et al. (2014). Insights on the Stellar Mass-Metallicity Relation from the CALIFA Survey. *Astrophysical Journal, Letters*, 791:L16.

Hirschmann, M. et al. (2015). The stellar accretion origin of stellar population gradients in massive galaxies at large radii. *Monthly Notices of the RAS*, 449:528–550.

Jimmy et al. (2015). The Gas Phase Mass Metallicity Relation for Dwarf Galaxies: Dependence on Star Formation Rate and H I Gas Mass. *Astrophysical Journal*, 812:98.

Kewley, L. J. and Ellison, S. L. (2008). Metallicity Calibrations and the Mass-Metallicity Relation for Star-forming Galaxies. *Astrophysical Journal*, 681:1183–1204.

La Barbera, F. et al. (2012). SPIDER - VII. Revealing the stellar population content of massive early-type galaxies out to 8R$_e$. *Monthly Notices of the RAS*, 426:2300–2317.

Lequeux, J. et al. (1979). Chemical composition and evolution of irregular and blue compact galaxies. *Astronomy and Astrophysics*, 80:155–166.

Lonoce, I. et al. (2015). Old age and supersolar metallicity in a massive z $\sim$ 1.4 early-type galaxy from VLT/X-Shooter spectroscopy. *Monthly Notices of the RAS*, 454:3912–3919.

Ly, C., Malkan, M. A., Rigby, J. R., and Nagao, T. (2016). The Metal Abundances across Cosmic Time (MACT) Survey. II. Evolution of the Mass-Metallicity Relation over 8 Billion Years, Using [OIII]4363AA-based Metallicities. *Astrophysical Journal*, 828:67.

Ma, X. et al. (2016). The origin and evolution of the galaxy mass-metallicity relation. *Monthly Notices of the RAS*, 456:2140–2156.

Maiolino, R. et al. (2008). AMAZE. I. The evolution of the mass-metallicity relation at z $\stackrel{>}{\sim}$ 3. *Astronomy and Astrophysics*, 488:463–479.

Naab, T., Johansson, P. H., and Ostriker, J. P. (2009). Minor Mergers and the Size Evolution of Elliptical Galaxies. *Astrophysical Journal, Letters*, 699:L178–L182.

Pastorello, N. et al. (2014). The SLUGGS survey: exploring the metallicity gradients of nearby early-type galaxies to large radii. *Monthly Notices of the RAS*, 442:1003–1039.

Peng, Y., Maiolino, R., and Cochrane, R. (2015). Strangulation as the primary mechanism for shutting down star formation in galaxies. *Nature*, 521:192–195.

Pettini, M. and Pagel, B. E. J. (2004). [OIII]/[NII] as an abundance indicator at high redshift. *Monthly Notices of the RAS*, 348:L59–L63.

Ramírez, I., Allende Prieto, C., and Lambert, D. L. (2013). Oxygen Abundances in Nearby FGK Stars and the Galactic Chemical Evolution of the Local Disk and Halo. *Astrophysical Journal*, 764:78.

Ryde, N. et al. (2016). Chemical Evolution of the Inner 2 Degrees of the Milky Way Bulge: $[\alpha/Fe]$ Trends and Metallicity Gradients. *Astronomical Journal*, 151:1.

Sánchez-Blázquez, P. et al. (2014). Stellar population gradients in galaxy discs from the CALIFA survey. The influence of bars. *Astronomy and Astrophysics*, 570:A6.

Sánchez-Menguiano, L. et al. (2016). Shape of the oxygen abundance profiles in CALIFA face-on spiral galaxies. *Astronomy and Astrophysics*, 587:A70.

Sanders, R. L. et al. (2015). The MOSDEF Survey: Mass, Metallicity, and Star-formation Rate at z $\sim$ 2.3. *Astrophysical Journal*, 799:138.

Santini, P. et al. (2014). The evolution of the dust and gas content in galaxies. *Astronomy and Astrophysics*, 562:A30.

Sato, K., Matsushita, K., and Gastaldello, F. (2009). Temperature and Metallicity in the Intra-Cluster Medium of Abell 262 Observed with Suzaku. *Publications of the ASJ*, 61:S365–S376.

Simionescu, A. et al. (2009). Chemical enrichment in the cluster of galaxies Hydra A. *Astronomy and Astrophysics*, 493:409–424.

Springel, V. and Hernquist, L. (2003). Cosmological smoothed particle hydrodynamics simulations: a hybrid multiphase model for star formation. *Monthly Notices of the RAS*, 339:289–311.

Steidel, C. C. et al. (2014). Strong Nebular Line Ratios in the Spectra of z $\sim$ 2-3 Star Forming Galaxies: First Results from KBSS-MOSFIRE. *Astrophysical Journal*, 795:165.

Steven, W. S. and Palla, F. (2008). *The Formation of Stars*. WILEY-VCH Verlag GmbH & Co. KGaA.

Tornatore, L., Borgani, S., Dolag, K., and Matteucci, F. (2007). Chemical enrichment of galaxy clusters from hydrodynamical simulations. *Monthly Notices of the RAS*, 382:1050–1072.

Tremonti, C. A. et al. (2004). The Origin of the Mass-Metallicity Relation: Insights from 53,000 Star-forming Galaxies in the Sloan Digital Sky Survey. *Astrophysical Journal*, 613:898–913.

Yabe, K. et al. (2015). The Subaru FMOS Galaxy Redshift Survey (FastSound). III. The mass-metallicity relation and the fundamental metallicity relation at z $\sim$ 1.4*. *Publications of the ASJ*, 67:102.

Zahid, H. J. et al. (2014). The FMOS-COSMOS Survey of Star-forming Galaxies at z $\sim$ 1.6. II. The Mass-Metallicity Relation and the Dependence on Star Formation Rate and Dust Extinction. *Astrophysical Journal*, 792:75.

Affirmation

I declare with this, I wrote this work on my own and I used no other sources and aids than those given in this work.

Munich, November 2016

_____

Emilio Mevius